Check for updates

Angewandte Chemie
www.angewandte.org

Zitierweise: *Angew. Chem. Int. Ed.* **2023**, *62*, e202219188
doi.org/10.1002/anie.202219188

Electrocatalysis

In Situ X-ray Absorption Spectroscopy of Metal/Nitrogen-doped Carbons in Oxygen Electrocatalysis

Bin Wu[+], *Tianxiao Sun*[+],* *Ya You*[+], *Haibing Meng*,* *Dulce M. Morales*, *Mailis Lounasvuori*, *Abbas Beheshti Askari*, *Li Jiang*, *Feng Zeng*, *Baoshan Hu*, *Xiangzhi Zhang*, *Renzhong Tai*,* *Zhichuan J. Xu*, *Tristan Petit*, and *Liqiang Mai**

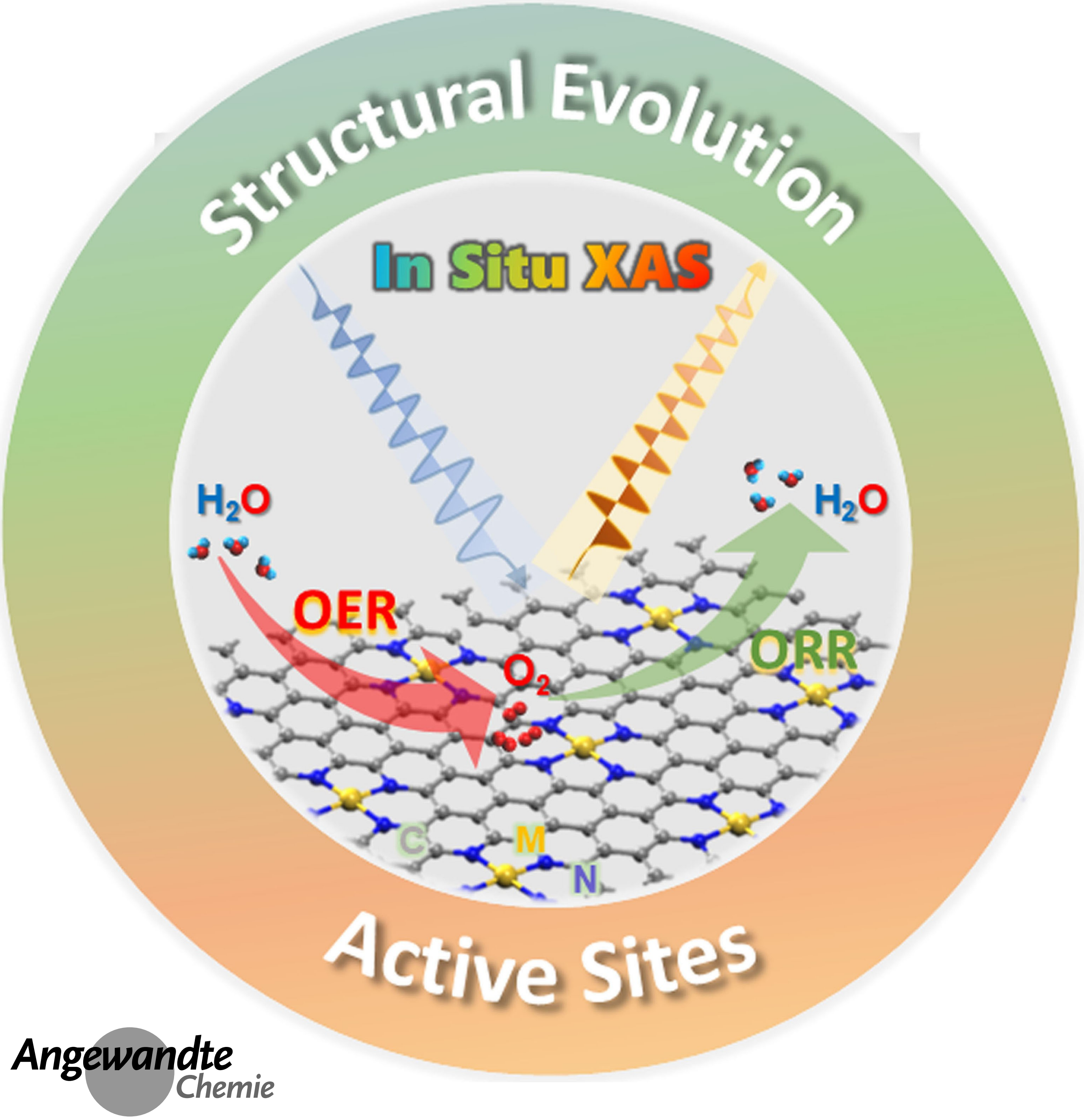

Abstract: Metal/nitrogen-doped carbons (M–N–C) are promising candidates as oxygen electrocatalysts due to their low cost, tunable catalytic activity and selectivity, and well-dispersed morphologies. To improve the electrocatalytic performance of such systems, it is critical to gain a detailed understanding of their structure and properties through advanced characterization. In situ X-ray absorption spectroscopy (XAS) serves as a powerful tool to probe both the active sites and structural evolution of catalytic materials under reaction conditions. In this review, we firstly provide an overview of the fundamental concepts of XAS and then comprehensively review the setup and application of in situ XAS, introducing electrochemical XAS cells, experimental methods, as well as primary functions on catalytic applications. The active sites and the structural evolution of M–N–C catalysts caused by the interplay with electric fields, electrolytes and reactants/intermediates during the oxygen evolution reaction and the oxygen reduction reaction are subsequently discussed in detail. Finally, major challenges and future opportunities in this exciting field are highlighted.

1. Introduction

Meeting increasing energy demand while lowering carbon emissions is one of the most daunting challenges in modern society, and can only be addressed with the aid of new sustainable energy technologies.[1,2] Oxygen electrocatalysis, comprising the oxygen reduction reaction (ORR) and the oxygen evolution reaction (OER), is the basis of industrial processes for various next-generation energy conversion and storage technologies, such as electrolyzers, fuel cells or rechargeable metal-air batteries, and therefore a crucial component of the energy transition to low carbon energy sources.[1] Nevertheless, the critical heterogeneous catalytic processes related to oxygen electrochemistry suffer from sluggish kinetics and pronounced overpotentials, leading to poor efficiency and high energy costs, thus hindering practical energy applications.[3] The development of sustainable electrocatalysts that enable the acceleration of the reaction rate with a low energy input, high selectivity and sufficient stability remains a major challenge.[4] On the one hand, noble metals, such as Pt-based electrocatalysts for the ORR and RuO_2/IrO_2-based electrocatalysts for the OER, show advantages such as high stability and good recyclability. However, potential commercial applications require to substantially reduce metal loading while maintaining a high catalytic activity, due to the high cost and low abundance of these precious metals.[5] On the other hand, earth-abundant transition metals and their oxides exhibit diverse crystalline structures and unique physicochemical properties, and have the advantage of cost-effectiveness, low price, satisfactory stability in alkaline conditions as well as a wide modulation potential for oxygen electrocatalysis.[6] Nevertheless, poor interfacial contact and mass transfer between catalysts and reactants/products, in addition to a poor electrical conductivity of metal oxides, become large obstacles for practical development of these materials.[7] Thus, to achieve wider commercialization of both noble and

---

[*] B. Wu,[+] T. Sun,[+] M. Lounasvuori, A. Beheshti Askari, T. Petit
Helmholtz-Zentrum Berlin für Materialien und Energie GmbH
Albert-Einstein-Straße 15, 12489 Berlin (Germany)
E-mail: tianxiao.sun@helmholtz-berlin.de

B. Wu[+]
Institute of Physics, Humboldt University Berlin
Newton-Straße 15, 12489 Berlin (Germany)

Y. You,[+] L. Mai
State Key Laboratory of Advanced Technology for Materials Synthesis and Processing, School of Materials Science and Engineering, Wuhan University of Technology
Luoshi Road 122, Wuhan 430070 (China)
E-mail: mlq518@whut.edu.cn

H. Meng
College of Chemistry, Taiyuan University of Technology
Taiyuan 030024 (China)
E-mail: menghaibing@tyut.edu.cn

D. M. Morales
Chemical Engineering group, Engineering and Technology institute Groningen (ENTEG), Faculty of Science and Engineering, University of Groningen
Nijenborgh 4, 9747 AG, Groningen (The Netherlands)

L. Jiang
CAS Key Laboratory of Molecular Nanostructure and Nanotechnology, CAS Research/Education Center for Excellence in Molecular Sciences, Institute of Chemistry, Chinese Academy of Sciences (CAS)
Beijing 100190 (China)

F. Zeng
State Key Laboratory of Materials-Oriented Chemical Engineering, College of Chemical Engineering, Nanjing Tech University
Nanjing 211816 (China)

B. Hu
College of Chemistry and Chemical Engineering, Chongqing University
Chongqing 401331 (China)

X. Zhang, R. Tai
Shanghai Synchrotron Radiation Facility, Shanghai Advanced Research Institute, Chinese Academy of Sciences
Shanghai 201204 (China)
E-mail: tairz@sari.ac.cn

Z. J. Xu
School of Materials Science and Engineering, Nanyang Technological University
50 Nanyang Avenue, Singapore 639798 (Singapore)

[+] These authors contributed equally to this work.

transition metal-based catalysts, it is vital to design advanced catalysts that overcome their inherent disadvantages.

Recently, metals incorporated into an N-doped carbon structure have emerged as potential sustainable oxygen electrocatalysts that provide high catalytic activity, high surface area and high electrical conductivity while allowing to reduce the amount of metal in the catalyst. In particular, metal supported on nitrogen-doped carbon (M–N–C, M referring to both noble and transition metals) materials are among the most promising candidates to replace conventional oxygen catalysts (Figure 1). Numerous studies have confirmed that the electron-accepting nitrogen dopant can not only modify the electron configurations of the active metal centers, but also create defects facilitating the adsorption and desorption of oxygen or water molecules as well as reaction intermediates such as *OH, *O and *OOH.[2] As a result, noble metals (Pt or Ru) loaded on nitrogen-doped carbon supports in the form of single-atom

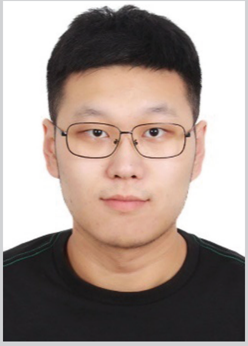

Bin Wu is a Ph.D. candidate at the Helmholtz-Zentrum Berlin für Materialien und Energie. He received his B.E. degree in Materials Chemistry from Chongqing University in China in 2016 as well as master degree in Materials Engineering from Institute of Chemistry, Chinese Academy of Sciences in 2019. His current research interests focus on in situ characterization of carbon nanomaterials for energy storage and conversion.

Tianxiao Sun, engaged in post-doctoral research at BESSY II light source, Helmholtz-Zentrum Berlin für Materialien und Energie, Germany; current main research directions are soft X-ray STXM, soft XAS, soft X-ray Ptychography and control system development and other related research; participated in the development of the new STXM of the 08 U line station of the Shanghai Synchrotron Radiation Source, and developed a new high signal-to-noise ratio absorption spectrum measurement system for 02B.

Ya You is a full professor in Wuhan University of Technology. She received her Ph.D. degree in Physical Chemistry from Institute of Chemistry, Chinese Academy of Sciences. After graduation, she worked as a postdoc fellow at the University of Texas at Austin. Her research focuses on materials design for electrochemical energy storage and conversion systems.

Haibing Meng received his Ph.D. in physical chemistry from Institute of Chemistry, Chinese Academy of Sciences, China (2019). From Sep. 2019 to Sep. 2021, he worked as a postdoctoral researcher in the Department of Chemical Engineering at Tsinghua University, China. Currently, he is an associate researcher in the College of Chemistry at Taiyuan University of Technology, China. His research interests focus on the design and fabrication of nanomaterials for gas adsorption and separation, electrocatalysis, and photocatalysis.

Renzhong Tai is a Vice President of Shanghai Advanced Research Institute, Chinese Academy of Sciences, Executive Deputy Director of Shanghai Light Source Science Center, Chief Scientist of Carbon Dioxide Photon Science Research Center of Shanghai Advanced Research Institute. His main research direction is the methodological research and application research of X-ray coherence in the fields of nanomicroscopy, nanofabrication, and dynamic characterization of nanocluster structures.

Tristan Petit leads the Young Investigator Group Nanoscale Solid-Liquid Interfaces at Helmholtz-Zentrum Berlin für Materialien und Energie. He obtained master degrees from ISAE-Supaéro, France and ETH Zürich, Switzerland in 2010 and a Ph.D. in Physics from ENS Cachan, France in 2013. He received a Freigeist Fellowship from the Volkswagen Foundation in 2015 and an ERC Starting Grant in 2020. His research focuses on in situ/operando spectroscopy of carbon nanomaterials and MXenes for energy conversion and storage applications.

Liqiang Mai is the Chair professor of Materials Science and Engineering at WUT, Dean of School of Materials Science and Engineering at WUT, Fellow of the Royal Society of Chemistry. He received his Ph.D. from WUT in 2004 and carried out his postdoctoral research at Georgia Institute of Technology in 2006–2007. He worked as an advanced research scholar at Harvard University and University of California, Berkeley. His current research interests focus on new nanomaterials for electrochemical energy storage and micro/nano energy devices.

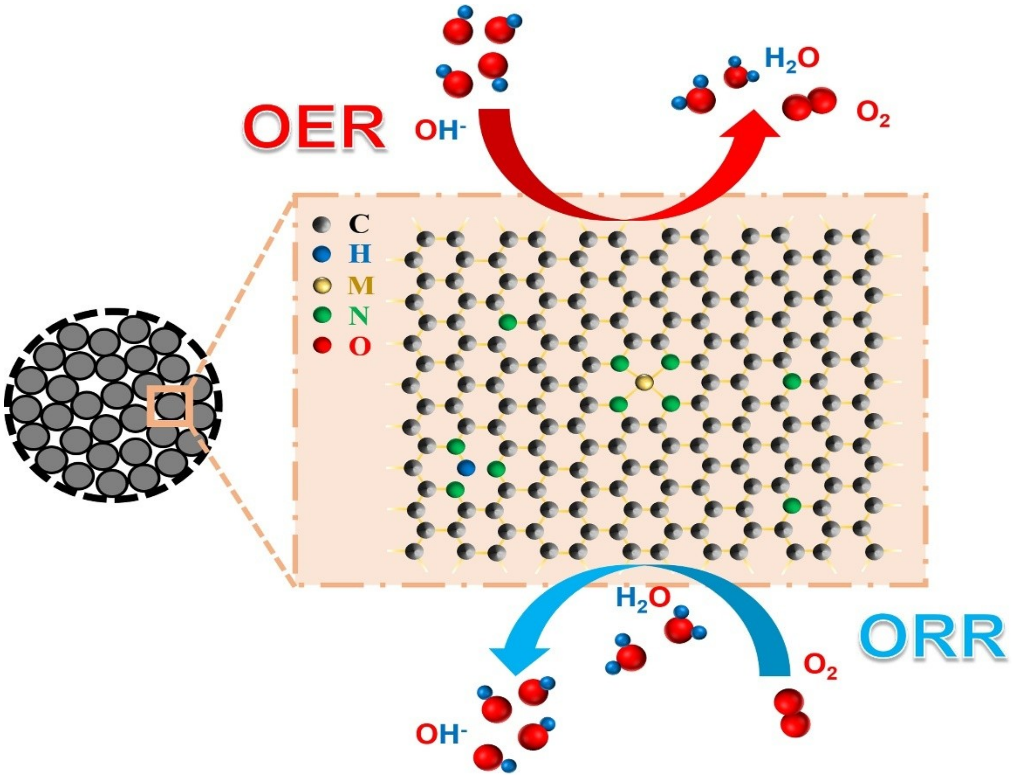

Figure 1. A schematic diagram on chemical configurations of M–N–C electrocatalysts illustrating their role as bi-functional catalyst for OER and ORR.

catalysts (SACs)-based M–N–C exhibit improved activity and stability toward the ORR compared to Pt nanoparticles.[8] SACs-based M–N–C materials with transition metals (M = Mn, Fe, Co, Ni, Cu) have also shown an optimal metal utilization by maximal exposure of active sites to these catalytic processes.[9] The formation of high-density homogeneously distributed single metal-N_x atomic sites over a highly graphitized matrix triggers a vastly improved activity in oxygen electrocatalysis, because the local electron density of metal-N_x active sites can be modulated by doping with N atoms in a carbon matrix.[10]

Owing to their well-defined active centers, the rational design of efficient M–N–C materials for catalysis can be achieved based on a molecular understanding of their catalytic mechanisms.[11] To this aim, X-ray absorption spectroscopy (XAS) serves as an essential tool to unravel the active site structures, geometric configurations and structural evolution.[12] The element-specificity of XAS is well-suited to single out the active sites in multi-element systems.[13] When carried out in situ, namely, probing the catalyst in an environment relevant to oxygen electrocatalysis, XAS provides key insights into activation/deactivation under reaction conditions, reaction intermediates and the role of the environment itself on the catalytic mechanisms.[14] Generally, extended X-ray absorption fine structure (EXAFS) is one of the most effective techniques for identifying the atomically dispersed M–N_x sites and providing information on atomic spacing and coordination number. In M–N–C materials, the EXAFS spectra can distinguish the metal-nitrogen coordination from the metal-metal bond and determine their coordination numbers. However, revealing the spatial arrangement of coordinated light elements surrounding the absorbing atom nucleus with EXAFS remains challenging. For this, X-ray absorption near edge structure (XANES) in the energy region that extends about 50–100 eV above the absorption edge can offer atomic information such as valence state, coordination number, and symmetry.[15] Thus, the information provided by in situ XAS (both EXAFS and XANES) is vital for future rational design of improved catalysts.[16] While in situ XAS is becoming a major technique for identifying the active sites and structural evolution of M–N–C materials for oxygen electrocatalysis, its use for monitoring reaction pathways has not been reviewed before to our knowledge. An overview of the role of metal-N_x as active sites in M–N–C-based oxygen electrocatalysts probed by in situ XAS and the correlation between structure and performance is still missing.

In this review, we comprehensively summarize the progress of in situ XAS for the characterization of structural changes and active sites in M–N–C materials over the last decade. First, an introduction to the fundamentals of XAS applied to oxygen electrocatalysis, including experimental details for in situ characterization under various electrochemical conditions is given. Then, representative studies highlighting active sites, structural evolution and structure-property-performance of M–N–C materials in oxygen electrocatalysis and the connection between in situ spectroscopic insights and catalytic mechanisms are summarized before presenting the most recent research progress related to in situ XAS investigation of M–N–C materials. Finally, an outlook of remaining challenges for in situ XAS characterization of M–N–C materials for oxygen electrocatalytic applications is proposed.

2. In situ XAS technique based on oxygen electrocatalysts

Directly characterizing the identity, coordination and structure of active species in M–N–C catalysts is often arduous due to the atomically dispersed active sites.[17] Additionally, the dynamic evolution of active sites in complex electrolyte environment makes the in situ characterization of M–N–C catalysts even more challenging. With its unique element discrimination ability, superior photon flux and well-suited probing depth, synchrotron-based in situ XAS is a valuable tool for the investigation and characterization of M–N–C-based oxygen catalysts, revealing complex structural information in atomic scale such as local geometry and electronic structure complementary to other X-ray-based techniques including powder X-ray diffraction (PXRD) and small-angle X-ray scattering (SAXS).[18] In most cases, the structure of the catalysts' active centers do not remain unchanged during the actual reaction process.[19] In particular, heterogeneous oxygen electrocatalysts often lose performance or self-regulate during the reaction.[20] Therefore, a comprehensive understanding of the dynamic reaction behavior of oxygen electrocatalysts is vital in studying catalyst mechanisms, such as the structural evolution of active sites.[21]

2.1. Fundamentals of XAS

XAS has become a widely used method for the investigation of the electronic and geometric structure of a given material with its fingerprint-like signature. Such signature originates from the excitation of electrons in the absorbing atoms to higher energy shells (Figure 2a), which leads to the sudden rise of the absorption cross-section at certain energy points referred to as absorption edges (Figure 2b). An in-depth discussion on the fundamentals of XAS is beyond the scope of this review and we refer the readers to relevant literature.[12] In this section, we present the basics of XAS in relation to the investigation of M–N–C materials.

According to the location relative to the absorption edge, to better interpret the oscillatory structure in the X-ray absorption cross-section, XAS is divided into XANES and EXAFS. The EXAFS region is a portion of an XAS spectrum starting 20–50 eV and extending to roughly 1000 eV beyond an absorption edge as shown in Figure 1c.[22] In this EXAFS region, photoelectrons are ejected from inner shells by resonant radiation, and the photoelectrons can be treated as spherical waves with a de Broglie wavelength comparable to the interatomic distance. The physical origin of EXAFS is the modulation of the absorption coefficient exhibited by the interference of the outgoing and back-scattered electron waves.[23] When the absorbing atom is surrounded by other neighboring atoms, the spherical wave of photoelectrons ejected from the absorbing atom will be scattered by the neighboring atoms and the back-scattered photoelectron waves will interfere with the outgoing wave. The maxima of oscillations in the EXAFS region result from constructive interference between these waves, and destructive interference leads to a minimum. In practice, EXAFS data obtained from experiments are often converted from $\mu(E)$ (in energy space) to $\chi(k)$ (in wave-number space) for subsequent quantitative analysis.[24] The XANES region starts at the first intense electronic transition allowed by the selection rules in the electric dipole approximation before the absorption edge and extends all the way to the beginning of EXAFS above it (Figure 2c).[25] Unlike EXAFS, XANES has an increased mean-free path

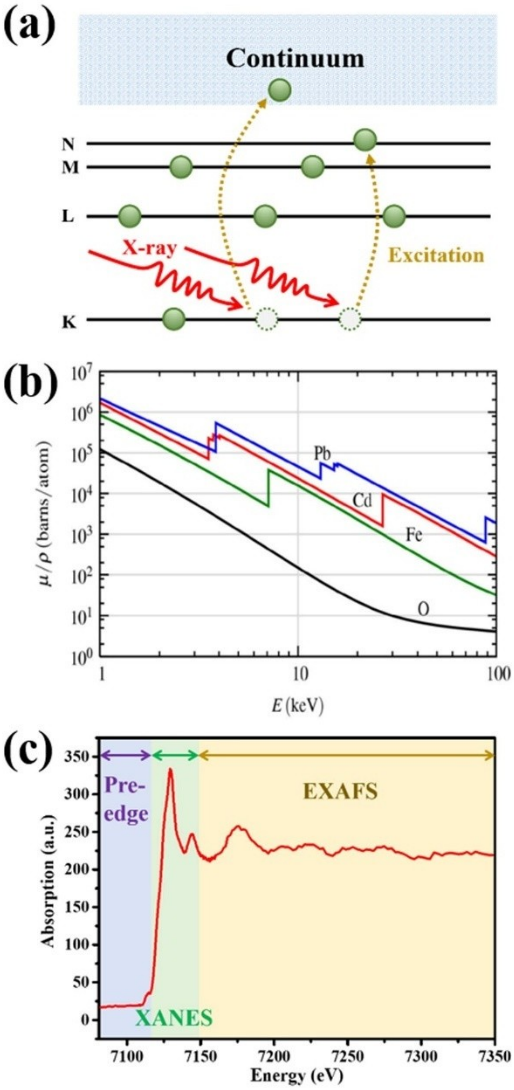

Figure 2. (a) Schematic diagram of electrons in an absorbing atom being excited by X-rays. (b) The mass attenuation coefficient μ/ρ for Fe, Cd and Pb over the x-ray energy range of 1 to 100 keV. (c) A schematic XAS spectrum, with XANES and EXAFS regions highlighted.

due to the low kinetic energy of emitted photoelectrons. The XANES structure is hence subject to a complex combination of both physical and chemical factors, making it more complicated to interpret than EXAFS but offering more structural information. The chemical shift of the main peak in the XANES of transition metal K-edge originates from changes of the oxidation state of the absorbing atom. In addition, the weak pre-edge peak has a quadrupole nature which can be used to identify localized structures around absorbing atoms.[26]

Moreover, X-rays are subdivided based on their energy into soft (with energies below 5 keV) and hard (with energies above 5 keV) X-rays. The soft X-ray energy band covers the K-edge of light elements and the L-edge of transition metal elements (such as Fe, Co, Ni, and Mn), which are all relevant for M–N–C catalysts. By contrast, hard X-rays cover the K-edge region of transition metals commonly used in oxygen electrocatalysts, where the pre-edge structure associated with the quadrupole transition can reflect the coordination symmetry of the metal sites.[27] Hard X-rays are able to penetrate thicker samples and thus are more easily implemented for in situ experiments. In addition, the energy intervals between absorption edges of different elements are relatively large in the hard X-ray band, which is well-adapted for the study of the long-range oscillation structure of EXAFS that provides information on the coordination and bond length of the probed atoms. The different measuring modes are described in more details in the subsequent section.

2.2. Experimental Methods for Structural Detection of M–N–C Catalysts

The continuous development of in situ XAS and related techniques have facilitated the elucidation of catalyst deactivation routes and the capture of oxidation state and local geometric coordination changes under reaction conditions, which is not possible via ex situ XAS experiments.[28] Due to three different detection modes (transmission, total fluorescence yield, and total electron yield), in situ XAS is a flexible and versatile technique for the exploration of the atomic structure, electronic structure evolution, and surface information of oxygen electrocatalysts.[29] In this part, we introduce the different XAS detection modes and describe the benefits and drawbacks of each modes.

2.2.1. Transmission Mode

The transmission mode is the most basic XASdetection method, and it is often used when bulk information of a sample is required. Figure 3a shows the experimental configuration for XAS experiment in transmission mode. In this setup, X-rays first pass through the front detector (e.g. gold mesh or photodiode) to record the light intensity I_0 of incident X-rays, and then the back detector (e.g. photodiode or photomultiplier tube) will record the transmitted light intensity I_1 through the sample. Typically, transmission detection shows excellent elemental discrimination on supported catalysts having metal loadings of at least 1 wt%. Therefore, it is well adapted to the detection of M–N–C catalysts under working conditions and has been applied in several XAS studies on Fe–N–C catalysts at the Fe K-edge.[30,31]

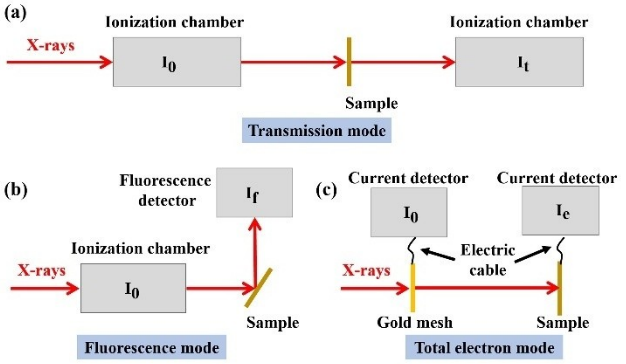

Figure 3. Schematic illustration of the XAS experiment setup in (a) transmission mode, (b) fluorescence mode, and (c) electron yield mode.

Note that the formation of active sites, intermediates and products during electrocatalytic processes takes place at the electrode/electrolyte interface. Thus, for in situ XAS experiments, particularly if conducted in transmission mode, samples with a high active surface area are required to ensure that enough signal is coming from the interfacial region.[32] When the thickness of the sample is not uniform, a part of the incident light is directly recorded by the back detector without being absorbed by the sample, which will reduce the amplitude or distort the XAS.[24] Therefore, the thickness of the sample needs to be uniform when preparing the sample. In addition, the atoms in the crystal are arranged in periodic arrays so that X-rays can be diffracted. When conducting XAS experiments on crystal samples in transmission mode, it is necessary to avoid the diffraction peaks of crystals, especially for samples with a low percentage of the element to be measured. Sometimes the intensity of the diffraction peaks is much higher than that of the absorption peaks.[33] The low X-ray penetration depth in the soft X-ray range implies that only samples with a thickness of 10—100 nm can be probed, thus greatly restricting the application range of XAS in the transmission mode.[22] Nevertheless, the high chemical sensitivity of XAS at the transition metal L-edge makes transmission in situ soft XAS worth developing.[12]

2.2.2. Fluorescence Yield Mode

For a catalyst sample with a low concentration of the element of interest, using conventional transmission mode may drown out the signal from the active metal center in a strong background. An effective solution is to use fluorescence yield (FY) mode to measure the absorption spectrum.[34] Typically, the fluorescence detection based on high energy resolution silicon drift detector (SDD) can reach the detection limit of ≈ 10 to $100\,\mu g\,g^{-1}$ in weight or $<1\,mmol\,L^{-1}$.[35] In FY mode (Figure 3b), the sample is generally at a 45-degree angle to the incident X-rays and the detector, which facilitates the direct collection of fluorescence photons emitted by the sample with a probing depth of ≈ 50 nm.[36] This geometry avoids spectral distortion caused by sample thickness and non-uniformity, making it well adapted to powdered samples such as M–N–C materials and was already applied for characterization at the Fe K-edge on Fe–N–C[37] or the Co K-edge for Co–N–C materials.[38]

Unfortunately, although the fluorescence yield is a linear function of the incident light intensity and absorption attenuation coefficient, XAS acquired with fluorescence detection often suffers from spectral line distortion caused by self-absorption effects, especially in the white line region of the absorption spectrum.[39] Avoiding self-absorption effects is, for example, feasible by diluting the analyte in the sample during sample preparation, or reducing the grain size for solid samples.[40] When the sample consists of nanoparticles with diameters of less than 10 nm, the dominant contribution to the absorption spectrum lies in the surface catalytic reaction.[41]

2.2.3. Total Electron Yield Mode

Total Electron Yield (TEY) mode is usually achieved by monitoring the drain current from the sample as a function of the excitation photon energy (Figure 3c). The detection depth of XAS measurements in TEY mode is governed by the mean free path of electrons, which can reach ca. 2–5 nm in the vicinity of the absorption of the element to be measured.[36] TEY mode therefore exhibits a high surface sensitivity.[42] The high electron yields (including secondary electron, Auger electron and photoelectron) for the absorption K-edges of light elements and L-edges of transition metals makes TEY-XAS ideal for surface information detection in the soft X-ray region.[43] On the other hand, heavy elements have very low electron yield at their K-edges, thereby making in situ XAS experiments in TEY mode difficult in the hard X-ray range.[44] While only conductive samples can be probed by TEY, it is still feasible to apply TEY to insulating bulk samples by grinding the sample into a powder and depositing it on a conductive substrate.[45] This strategy effectively suppresses the sample charge-up distortion. This may be relevant for M–N–C materials and has been successfully applied at the Fe L-edge and Fe and N K-edges of Fe–N–C materials[46,47] In situ TEY-XAS remains challenging because the short mean free path of electrons is hardly compatible with liquid environment.

2.3. Applications of in situ XAS for Oxygen Electrocatalysis

The oxygen electrocatalyst is a complex, dynamic entity, and therefore challenging to probe under reaction conditions via in situ XAS experiments. Oxygen electrocatalysts undergo chemical absorption and electron transfer during the reaction, resulting in a change of the metal oxidation state and orbital occupancy of the active species. These electronic properties have been probed by in situ XAS techniques. Hard X-ray XAS, especially in FY and transmission mode are most frequently used for in situ studies of oxygen electrocatalysts. Since the original in situ cell model proposed by Lytle et al. in 1979,[48] many in situ cells have been introduced with the popularization of synchrotron light sources. Typically, Kapton foil and Si_3N_4 membranes are employed as windows for hard and soft X-rays, respectively, to guarantee the electrochemical cell being leak-tight.[49] Electrocatalysts are generally deposited onto a porous carbon-based working electrode (such as carbon cloth and carbon paper) to avoid interference with the signal acquisition. Figure 4a–c are schematic diagrams of in situ electrochemical cells operating in different modes.[50] In transmission mode (Figure 4a), since the detector records the intensity of the transmitted light from the sample, the electrochemical cell must have two X-ray windows. In order to suppress the influence of the electrolyte on the effective signal, the electrochemical cell usually allows to adjust the electrolyte thickness in the X-ray propagation direction. An electrolyte layer thickness less than 1 mm is usually required to avoid strong absorption of X-rays. In contrast, in FY mode (Figure 4b) and TEY mode (Figure 4c), sample information is collected by a fluorescence detector or a gold electrode on the same side of the cells exposed to X-rays. These cells, which require only one X-ray-transparent window, tend to tolerate larger electrolyte thicknesses.

To eliminate the interference caused by the presence of gas bubbles in the electrolyte, or their evolution during catalytic reactions, some electrochemical cells are equipped with pumps that flow the electrolyte, thus removing the bubbles from the catalyst surface. For example, Yang and collaborators designed an in situ electrochemical cell based on detecting transmitted X-rays to explore the active center evolution of a Co-based catalyst during ORR under working conditions.[51] The three-electrode cell consisted of a 40-µm-thick electrocatalyst layer on a 200-µm-thick carbon paper as the working electrode, Ag/AgCl as the reference electrode, a carbon rod as the counter electrode, and a 1.0 M KOH solution as the electrolyte (Figure 4d). The frame of the electrochemical cell is made of chemically inert Teflon, and the thickness of the electrolyte layer can be adjusted to less than 200 nm to suppress the interference of the electrolyte on the effective transmission signal. Thus, the authors successfully captured the dynamic changes of active sites under realistic conditions with this transmission cell. Furthermore, Görlin et al. reported an in situ electrochemical cell to examine the effect of Fe on the redox activity of the Fe–Ni catalyst under applied bias (Figure 4e).[52] The working electrode consists of a 300-nm-thick sample film electro-deposited on a 35-µm-thick graphene sheet and bonded together by Kapton tape, where the copper sheet is in contact with the working electrode from the graphene side, while the sample layer is directly immersed in the electrolyte. Experiments confirm that this electrochemical

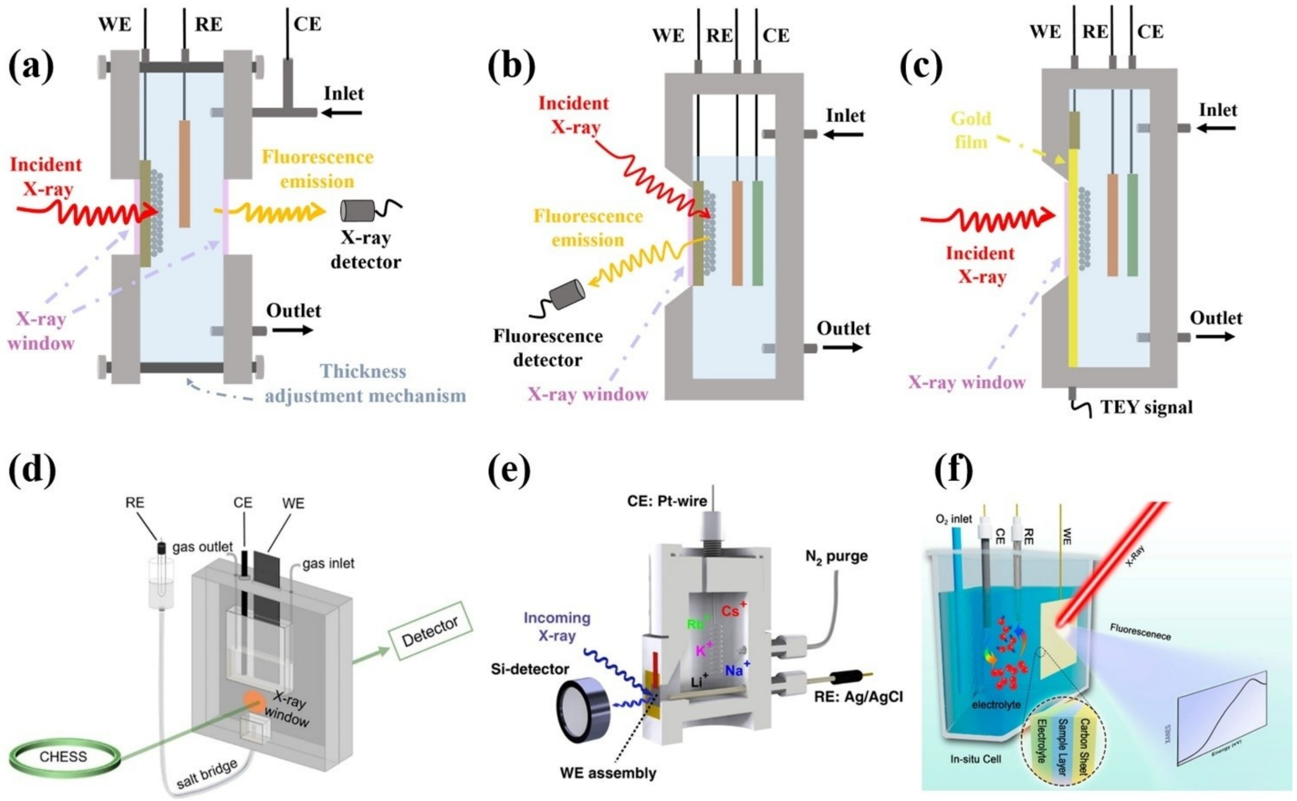

Figure 4. Schemes of in situ XAS electrochemical cells for (a) transmission mode, (b) fluorescence yield mode, and (c) electron yield mode. WE: working electrode. RE: reference electrode. CE: counter electrode. (d) Illustration of the in situ XAS electrochemical cell for transmission mode. (Reproduced with permission from [51], copyright 2019, American Chemical Society). (e) Schematic of in situ XAS electrochemical cell for fluorescence yield mode. (Reproduced with permission from [52], copyright 2020, Springer Nature). (f) Illustration of the in situ XAS electrochemical cell for fluorescence yield mode. (Reproduced with permission from [53], copyright 2020, American Chemical Society).

cell design can be effectively applied to in situ XAS experiments in the FY mode to explore the catalytic mechanism in OER or ORR processes.

These electrochemical cells play a pivotal role for in situ XAS characterization of M–N–C catalysts. For example, Li et al. studied the dynamic evolution of active sites in Fe–N–C SACs during the catalytic process by in situ XAS using such an electrochemical cell with Kapton tape as the X-ray window to prevents the leakage of the internal 0.1 M KOH or 0.1 M $HClO_4$ electrolyte.[54] Catalyst samples were deposited on carbon-fiber electrodes to form working electrodes, while reference and counter electrodes were made of SCE and Pt, respectively. Both in situ XANES and EXAFS spectra of the Fe–N–C SAC were collected at the Fe K-edge. The experimental results successfully uncover the role of the N–FeN_4C_{10} moiety as the active site in ORR process. Similarly, to investigate the dynamic structure change of Mn–N_2C_2 atomic interface sites in a carbon-based isolated Mn–N_x bifunctional electrocatalyst (denoted as Mn SAC) during ORR and OER, Shang et al. proposed an electrochemical cell for in situ XAS in FY mode (Figure 4f).[53] The in situ cell uses carbon cloth to separate the internal 0.1 M KOH electrolyte from the external environment and acts as a window for incident hard X-rays and fluorescence emission. The Mn SAC sample is placed directly on the side of the X-ray window facing the electrolyte, which simultaneously assumes the function of the working electrode, thereby reducing the attenuation of the fluorescence signal. As a result, they elucidated that the Mn^{2+}–N_2C_2 and Mn^{4+}–N_2C_2 moieties of Mn SAC act as active center in the ORR and OER processes, respectively.

With its local structure sensitivity and excellent spatial resolution, model-based EXAFS analysis allows the estimation of atomic structures of small ensembles, providing knowledge on the evolution of electrocatalyst structures during reactions. While EXAFS allows access to the coordination environment of the reactive centers in the electrocatalysts, in situ XANES analysis can reveal the oxidation state of the active centers under working conditions. Overall, the in situ XAS technique contributes to the understanding of the correlation between the structural transformation and stability/activity of electrocatalysts during the ORR and OER processes as discussed in more details in the following sections.

3. Active Sites and Structural Evolution of M–N–C-based Oxygen Electrocatalysis

The practical applications of energy conversion and storage technologies, such as water-splitting devices, proton exchange membrane fuel cells (PEMFCs) and zinc-air batteries (ZABs), have been hindered by the unsatisfactory performance of oxygen electrocatalysts due to the sluggish reaction kinetics of anodic OER and cathodic ORR.[55] As discussed in the introduction, M–N–C materials have attracted considerable attention for these reactions. A wide variety of N-doped carbon-based catalysts such as single atomic, dual single atomic, atomic clusters and metal nanoparticles have been synthesized.[56] In this section, we briefly review the structure–property relationship and possible M–N–C active sites that are currently discussed in the literature based on electrochemistry before focusing more specifically on the specific insights offered by in situ XAS in the section 4.

3.1. Structure-Property Effects for M–N–C Catalysts

The oxygen electrocatalytic performance of M–N–C catalysts is influenced by several factors such as electrical conductivity, porosity, and the synergistic interaction between metal species and carbon substrates.[57] The metal active sites play a leading role in modulating the activity, stability and selectivity of M–N–C catalysts. Therefore, much effort has been devoted to investigating their corresponding structure-property for oxygen electrocatalysis. Many M–N–C catalysts have been synthesized to correlate electrocatalytic performance with the properties of their active sites. In general, active sites of M–N–C-based catalysts tend to form $\mathrm{M{-}N_x}$ structures and/or M–M bonds. An overview of the ORR/OER performance and the primary active sites of the various M–N–C-based electrocatalysts reviewed in this section is summarized in Table 1.

3.1.1. Single Metal Site Effect

The oxygen electrocatalytic performance of M–N–C SACs can be modulated by the coordination environments of single metal sites. For instance, Zhang et al. fabricated high-purity pyrrole-type $\mathrm{Fe{-}N_4}$ ORR electrocatalysts with superior performance for PEMFCs.[68] This pyrrole-type $\mathrm{Fe{-}N_4}$ catalyst exhibited an ultrahigh active area current density of $6.89\ \mathrm{mA\,m^{-2}}$ in an acidic medium, outperforming that of most reported M–N-based ORR catalysts. EXAFS analysis uncovered that the atomic/electronic structures of $\mathrm{Fe{-}N_4}$ sites are effectively modulated by the high-purity pyrrole-type coordination, thereby resulting in superior ORR performance (Figure 5a–c). In 2020, Ma et al. obtained atomically dispersed Cu catalysts (Cu SACs) with different coordination structures.[69] The Cu active centers were modulated by controlling the pyrolysis temperature. The Cu SACs with $\mathrm{Cu{-}N_3}$ moieties pyrolyzed at 900 °C exhibited outstanding ORR performance with a high $E_{1/2}$ of 0.87 V (vs. RHE) and a turnover frequency of 0.16 Hz, attributed to the favorable formation of $\mathrm{O_2^*}$ intermediate on $\mathrm{Cu{-}N_3}$ compared to $\mathrm{Cu{-}N_4}$ moieties. In 2021, Li et al. synthesized a single Fe site catalyst (Fe–N/S–C) by embedding single Fe sites within N, S co-doped carbon nanosheets by chemical vapor deposition (CVD).[70] The N, S co-doping optimizes the charge distribution of Fe sites and imparts Fe–N/S–C with high surface areas and porosity.

3.1.2. Bimetal Site Effect

By introducing a second metal site into the single-atom catalysts, a larger modulation of the M–N–C structure is

Table 1: Summary of common active sites of M–N–C materials and their ORR and OER performance. $E_{1/2}$ vs. RHE (V) and E_{10} vs. RHE (V) represent the half-wave potential (ORR) and potential at a current density of $10\ \mathrm{mA\,cm^{-2}}$ (OER), respectively. NC = N-doped carbon; Fe-14MR = $\mathrm{Fe^{II}}$ 1,14 : 7,8-ditethenotetrapyrido-[2,1,6-de:2′,1′6′-gh:2″,1″,6″-kl:2‴,1‴,6‴-na [1,3,5,8,10,12]hexaazacyclotetradecine; NCTNs = N-doped carbon nanotubes; Int-PtNiN/KB = N-doped ordered intermetallic PtNi nanocatalysts supported by Ketjenblack; GCs = N-doped graphene-like hierarchically porous carbon nanosheets.

Catalyst	Reaction	Electrolyte	Active sites/species	$E_{1/2}$ vs. RHE [V]	E_{10} vs. RHE [V]	Ref.
Cu/Zn–N–C	ORR	0.1 M KOH	$\mathrm{Cu{-}N_4/Zn{-}N_4}$	0.83	–	[58]
$\mathrm{Fe_2N_6/C}$	ORR	0.5 M $\mathrm{H_2SO_4}$	$\mathrm{Fe^{2+}{-}Fe^{2+}}$	0.84	–	[59]
Fe–N–C	ORR	0.1 M KOH	$\mathrm{Fe{-}N_x}$	0.88	–	[10]
$\mathrm{Fe{-}N_x{-}C}$	ORR	0.1 M $\mathrm{HClO_4}$ and 0.1 M KOH	$\mathrm{Fe^{2+}{-}N_4}$	0.85–0.87	–	[37]
Fe-14MR/C	ORR	0.5 M $\mathrm{H_2SO_4}$	$\mathrm{Fe^{2+}{-}N_4}$	0.75	–	[30]
PtNi–N/C	ORR	1 M $\mathrm{HClO_4}$	$\mathrm{(Pt_xNi_{1-x})_4N}$	0.93	–	[60]
$\mathrm{Ni_1{-}NC}$	ORR	0.1 M NaOH	$\mathrm{Ni_1^{(2\text{-}\delta)+}N_2}$	0.92	–	[61]
Co–N–C	ORR	0.5 M $\mathrm{H_2SO_4}$	$\mathrm{Co{-}N_4}$	0.81	–	[62]
Zn/Co–N–C	ORR	0.1 M KOH	$\mathrm{ZnCoN_6(OH)}$	0.86	–	[63]
Ni@Ni–NC	OER	1.0 M KOH	$\mathrm{Ni{-}N_4}$	–	1.51	[64]
$\mathrm{Co{-}N_4{-}GCs}$	OER	0.1 M KOH	$\mathrm{Co{-}N_4}$	–	1.58	[65]
$\mathrm{CoO_x@CoN_y/NC}$	OER	0.1 M KOH	$\mathrm{Co_4{-}N}$	–	1.69	[66]
Mn–N–C	OER and ORR	0.1 M KOH	$\mathrm{Mn^{4+}{-}N_2C_2}$	0.915	1.58	[53]
Co/Co–N–C	OER and ORR	0.1 M KOH	Co–Co/Co–N (ORR) and Co–O (OER)	0.82	1.54	[38]
CoFe/3D NC	OER and ORR	0.1 M KOH	Fe–Fe and Co–Co	0.91	1.79	[67]

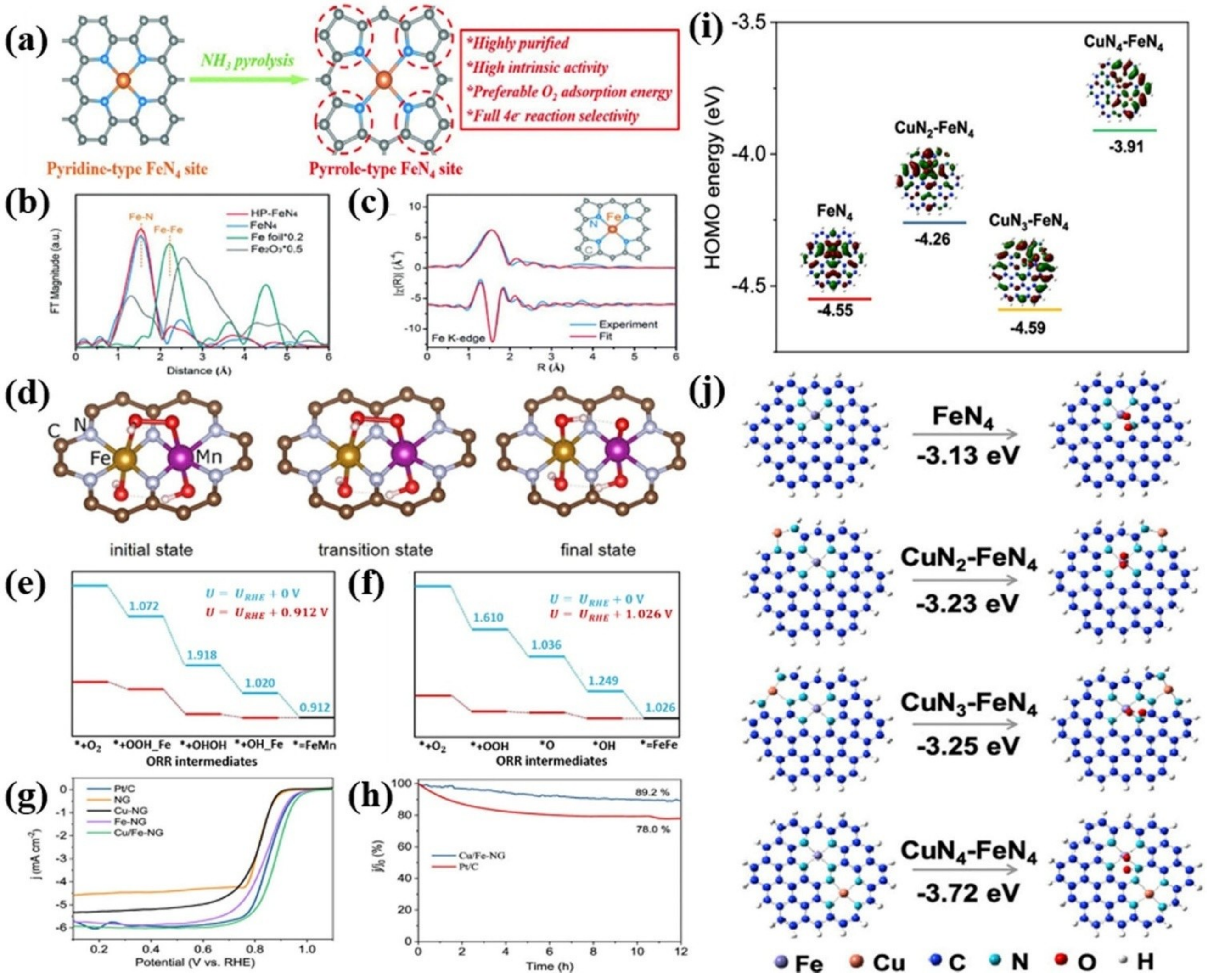

Figure 5. Structure of active sites in M–N–C -based oxygen electrocatalysis (a) Preparation process of high-purity pyrrole-type FeN_4 structure. Grey, blue and orange spheres represent C, N and Fe atoms, respectively, (b) Fourier transformations of the EXAFS spectra for Fe foil, Fe_2O_3, HP–FeN_4 and FeN_4 and (c) First-shell fitting of Fourier transformations of EXAFS spectra for HP–FeN_4. Top and bottom spectra are magnitude and imaginary part, respectively. Inset: The structure of the iron site in the HP–FeN_4 material. (Reproduced with permission from [68], copyright 2020, The Royal Society of Chemistry). (d) The splitting of absorbed *OOH on $FeMnN_6$ cluster with an energy barrier of 0.10 eV. The absorbed *OOH in the "laying down" configuration, the transition state and the split *OOH, (e) The theoretical Gibbs free energy profile for the ORR process on OH-decorated $FeMnN_6$, (f) The theoretical Gibbs free energy profile for the ORR process on OH-decorated Fe_2N_6 clusters embedded within a graphene lattice. (Reproduced with permission from [71], copyright 2022, WILEY-VCH Verlag GmbH & Co. KGaA, Weinheim). (g) LSV curves of the as-prepared catalysts and Pt/C, (h) Chronoamperometric responses of Cu/Fe–NG and Pt/C, (i) HOMO energy levels on four different models, (j) Computational models, O_2 adsorption configurations, and corresponding adsorption energies for FeN_4 and CuN_x–tFeN_4 ($x=2, 3, 4$). (Reproduced with permission from [72], copyright 2020, American Chemical Society)

possible. In 2020, Chen et al. prepared dual single-atomic Ni–N_4 and Fe–N_4 sites on the inner and outer walls of graphene hollow nanospheres (GHSs) by a step-by-step self-assembly method.[73] In this Ni–N_4/GHSs/Fe–N_4 Janus catalyst, the outer Fe–N_4 moieties are highly active towards the ORR while the inner Ni–N_4 clusters contribute to an excellent OER activity. In 2021, Luo et al. modulated the coordination environment of Ni single-atom catalysts for improving the catalytic behavior by a secondary single-atom regulation method.[74] The introduction of atomically dispersed Fe moieties increases the Ni–N/O coordination number by the long-range electronic interaction, optimizing the adsorption energies of active sites and reaction intermediates. The resultant dual atom catalyst FeNi–SAs@NC exhibits an exceptional catalytic OER activity with an overpotential of 298 mV (vs. RHE) at 10 mA cm^{-2}, surpassing the benchmark IrO_2 (313 mV vs. RHE). Recently, Cui et al. harvested a novel dual single-atom catalyst (FeMn-DSAC) by combining adjacent Fe–N_4 with Mn–N_4 sites supported on 2D ultrathin porous N-doped carbon nanosheets.[71] It displays outstanding OER/ORR bifunctional catalytic activities. Theoretical investigations reveal that the synergistic Fe/Mn dual sites of $FeMnN_6$ favor the *OOH dissociation. This unique configuration with the

*OOH "lying down" on top of the $FeMnN_6$ cluster is beneficial for intermediate dissociation (Figure 5d, 5e and 5f). Additionally, Li et al. prepared FeCo–N-doped hollow carbon nanocages (FeCo–N–HCN) with neighboring $Fe–N_4–C$ and $Co–N_4–C$ dual active centers for ORR catalysis.[75] DFT calculations reveal that the dual active sites reduce the energy consumption of the *OH removing step, resulting in a smaller overpotential in the whole process and therefore synergism of neighboring $Fe–N_4–C$ and $Co–N_4–C$ leading to a decreased energy barrier for ORR.[75]

3.1.3. Atomic Cluster Effect

The size of an atomic cluster lies between single atoms and nanoparticles, demonstrating novel structures that could allow enhanced catalytic performance.[72] For example, Xu et al. synthesized Cu nanocluster/FeN_4 species within N-doped graphene (Cu/Fe–NG) through a simple vacuum-annealing approach.[72] The authors found that the amorphous Cu/FeN_4 composites provide the high-activity active centers of bimetallic Cu/$Fe–N_x$ sites for ORR. As a result, the Cu/Fe–NG catalyst shows high ORR activity with a high $E_{1/2}$ of 0.88 V (vs. RHE), long-time durability, and low H_2O_2 selectivity (Figure 5g and 5h). The DFT data reveal that the co-existence of $Fe–N_4$ and $Cu–N_x$ moieties in Cu/Fe-NG facilitates the adsorption and activation of the O_2 molecules (Figure 5i and 5j). Additionally, Luo et al. recently fabricated non-noble metal-based bifunctional catalysts composed of Ni single atoms, Fe single atoms, and NiFe nanoalloys embedded into carbon nanotubes (NiSAFeSA-Ni_xFe/CNT).[76] Due to the structure properties, the optimized NiSAFeSANi_{50}Fe/CNT catalyst presents an ultra-low overpotential of 227 mV at 10 $mA\,cm^{-2}$ toward OER.

3.2. Modulation of Coordination Configurations Induced by Metal-Nitrogen Bonding

Different coordination configurations can be obtained by modulating the metal-nitrogen bonding. The N coordination number, coordination type, and metal atom coordination directly influence the catalytic performance.[77] Thus, many pioneering works have been devoted to constructing various coordination configurations of M–N–C catalysts to enhance their electrocatalytic performance and reveal the related mechanism, which in turn promotes the development of high-efficiency oxygen electrocatalysts.

3.2.1. Modulation of N Coordination Number

By changing the synthesis strategy, the N coordination number can be precisely modulated to control the catalytic activity of metal sites.[78] In 2022, Xue et al. realized the electron spin-state modulation of Fe active centers in SACs-based Fe–N–C ranging from a low-spin state (LS) for FeN_5 ($Fe–N_5$–LS) to a high-spin state (HS) for FeN_4 ($Fe–N_4$–HS) and FeN_3 ($Fe–N_3$–HS) by converting defect-rich pyrrolic N-coordinated FeN_x sites, which tune the electron readily penetrating the antibonding π-orbital of oxygen.[79] The designed $Fe–N_4$–HS catalyst with high spin state ($S_{5/2}$) displays excellent acidic/alkaline ORR activity (Figure 6a). Moreover, Li et al. obtained a Fe single-atom catalyst (Fe–N–C/rGO SAC) by pyrolyzing the hybrid of ZIF-8 and graphene oxide (GO).[80] DFT and activity measurement revealed that the Fe site features the $Fe–N_5$ structure with four equatorial and one axial N atoms, inducing its asymmetric electron distribution and promoting the generation of reactive intermediates. Recently, Zaman et al. utilized a scalable molten-salt strategy to prepare a low platinum (Pt) nanoalloy implanted in an M–N-graphene catalyst.[81] DFT calculations reveal that the nanoalloys embedded into graphene substrates with $Co–N_4$ and $Pt–N_4$ coordination types feature higher catalytic activity than the one with $Co–N_3$ and $Pt–N_3$ coordination types. Combined with the synergistic coupling of different active species, the platinum-alloyed graphene catalyst exhibits an outstanding ORR performance with E_{onset} and $E_{1/2}$ of 1.05 and 0.9 V vs. RHE, respectively.

3.2.2. Modulation of Coordination Type

To pursue the enhancement of catalytic performance of oxygen electrocatalysts, many researchers have concentrated their efforts on developing M–N–C catalysts with different coordination types to optimize the electronic structures and absorption energies of metal sites. In 2019, Zhang et al. fabricated different single metal atoms supported on N, S-codoped carbon (NSC) and investigated their structure and catalytic performance as ORR catalysts.[82] Their characterization, including TEM and EXAFS, revealed that the Fe/Co/Ni-centered single-atom catalysts (Fe–SAs/NSC, Co–SAs/NSC and Ni–SAs/NSC) possess different structures, as different hybrids, composed of the metal ion and the N, S-containing precursors, are formed during the initial synthesis process (Figure 6c–t). Briefly, the Fe–SAs/NSC features FeN_4S_2-type active sites with S atoms bonding with the N atoms. For Co–SAs/NSC and Ni–SAs/NSC, the S atoms bond with metal atoms, inducing CoN_3S_1 and NiN_3S_1 center sites as shown in Figure 6b. Theoretical data disclosed that the FeN_4S_2 presents higher charge density and lower energy barriers towards the formation of the intermediates and products involved, which are more active than CoN_3S_1 and NiN_3S_1. In 2021, Yang et al. obtained the atomically dispersed $Fe–N_4$/C catalysts (Fe/SNCFs–NH_3) and deposited them on a free-standing carbon fiber membrane used in a Zinc-air battery.[83] The large specific surface area enhances the accessibility of $Fe–N_4$/C sites on the carbon substrate. Additionally, the S doping can modulate the configurations of Fe sites in Fe/SNCFs-NH_3, inducing its excellent bifunctional OER/ORR activities. Recently, Huang et al. encapsulated CoN_4Cl, $CoCN_3Cl$, and CoC_4Cl within graphene substrate to investigate their properties toward oxygen electrocatalysis.[84] The catalyst with $CoCN_3Cl$ configuration exhibits higher OER performance with an overpotential of 359 mV at 10 $mA\,cm^{-2}$ compared with catalysts with the

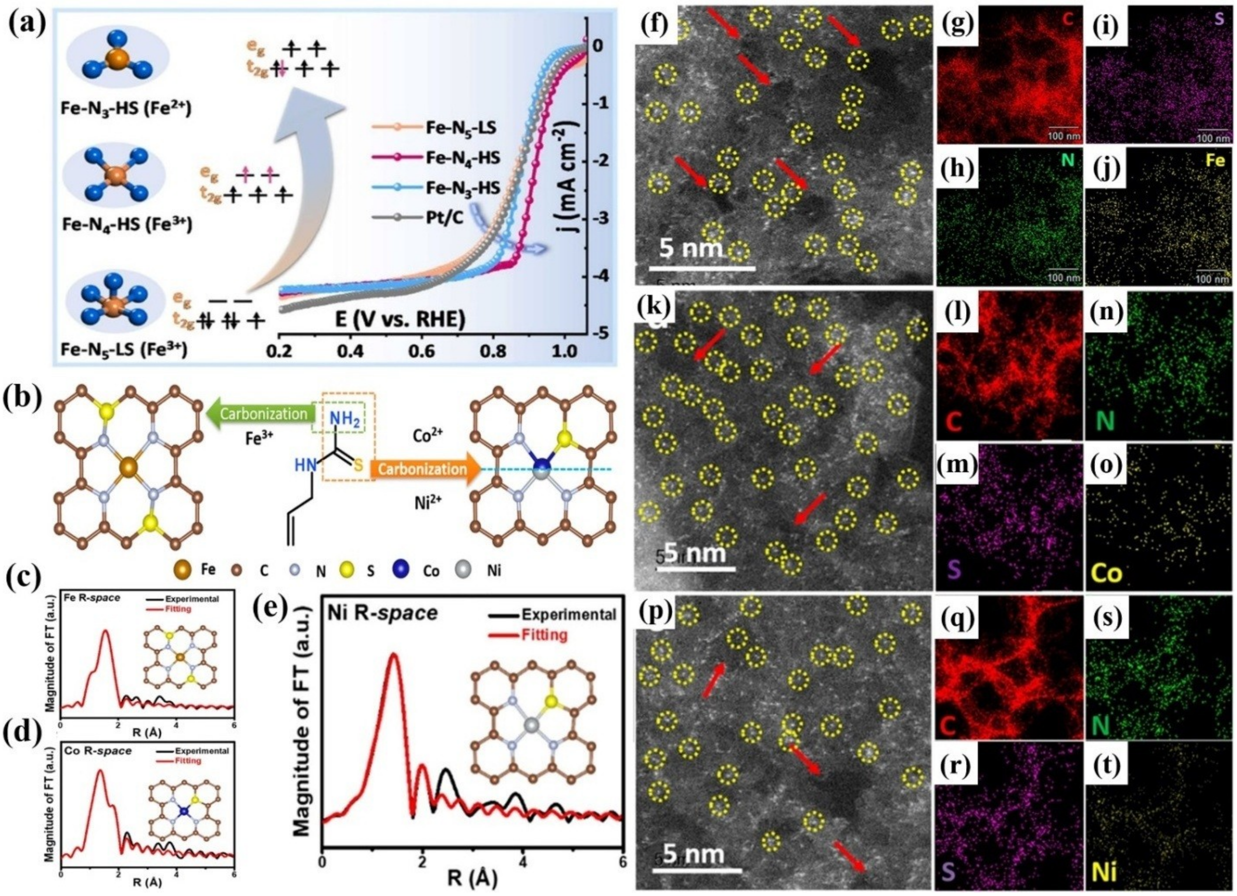

Figure 6. Structure of active sites in M–N–C -based oxygen electrocatalysis (a) The electron spin-state modulation of Fe active centers in SACs-based Fe–N–C identified by activity measurement and theoretical calculations. (Reproduced with permission from [79], copyright 2022, Elsevier). (b) The schematic illustration of the formation of Fe-SAs/NSC, Co-SAs/NSC, and Ni-SAs/NSC with different coordination environments, (c–e) EXAFS curves between the experimental data and the fit of (c) Fe-SAs/NSC, (d) Co-SAs/NSC, and (e) Ni-SAs/NSC. The insets are the fitted structures, (f, k, p) HAADF-STEM image of Fe-SAs/NSC, Co-SAs/NSC and Ni-SAs/NSC, showing the single atoms and in-plane pores (red arrows), (g–j, l–o, q–t) HAADF-STEM elemental distribution of the C, N, S, Fe, Co and Ni elements in M-SAs/NSC (M = Fe, Co, Ni). (Reproduced with permission from [82], copyright 2019, American Chemical Society)

CoC_4Cl (396 mV) and CoN_4Cl (> 500 mV) structures. DFT calculations indicated that the stronger binding strength for Co=O* in these structures facilitates the kinetics of the rate-determining step and, thus, the OER efficiency. Hence, the Co site with the CN_3Cl structure possessed the optimized binding strength of Co=O*.

4. Investigations on M–N–C-based Oxygen Electrocatalysts by in situ XAS

The sensitivity of XAS to bond lengths and bond strengths between catalyst and adsorbate has been widely used to rationalize the structure–property relationship in the materials for the OER and the ORR.[16] However, in many of these cases, the actual active species and the working mechanism of the oxygen electrocatalysts remain actively debated owing to the coexistence of species with different oxidation states and chemical environments as well as the difficulty of probing them due to the rapid transformations of the electronic and atomistic structure under reaction conditions.[12] In situ XAS studies can provide insight into the local changes around metal centers in the catalysts that can be used to gain a mechanistic understanding of the OER and ORR processes.[85] In particular, M–N–C-based oxygen catalysts have been proven as promising candidates to improve OER and ORR performance effectively, however, the identification of catalytic mechanisms, structural evolution and active sites of this class of materials by in situ XAS are rather rare.[12] In this section, we introduce some typical cases related to noble and non-noble M–N–C-based oxygen electrocatalysts investigated by in situ XAS.

Nanoscale catalysts have been rapidly moving to SACs M–N–C materials with enhanced activity and improved selectivity due to their large surface-to-volume ratio.[86] However, the development of such electrocatalysts still have inevitable limitations owing to their ultra-low mass loading and mostly amorphous structure.[87] This presents a technical difficulty for most characterization methods to study the structural information and the evolution of the associated active sites of such atomically dispersed catalysts. EXAFS becomes one of the best strategies for characterizing M–N–C materials, with its sub-Ångstrom spatial resolution and elemental specificity. Furthermore, when the particle size of the catalyst is reduced, more surface atomic sites are involved in the catalytic reaction compared to larger particles and bulk-sensitive in situ XAS can become sensitive to interfacial phenomena.

4.1. Noble Metal–N–C Materials

In energy, chemical and metallurgical production processes, noble metal catalysts are widely used due to their intrinsic performance for oxygen electrocatalysis. The promotion strategy of combining nitrogen doping and a suitable carbon support further enhances the selectivity, activity and stability of noble metal catalysts in ORR, particularly for the M–N–C single atom configuration, which has brought new research impetus towards noble metal catalysts. Thanks to in situ XAS, researchers gained the ability to study the oxidation susceptibility and the structural properties of the noble metal catalysts as a function of applied potential.

For example, compared with conventional nanoparticle-type catalysts, smaller-sized SACs further improve the utilization efficiency of active metal species and exhibit outstanding catalytic activity and selectivity. Recently, Li and co-workers employed the in situ XAS technique with potentials ranging from 0.4 V to 1.1 V (vs. RHE) to investigate the difference in chemical behavior of an N-doped C-supported high-loading Pt SAC (Pt_1/NCNS) and its nanoparticle counterpart (Pt–SNs/NCNS) during the ORR.[88] In situ XAS results are shown in Figure 7a–d. In the XANES at Pt L_3 edge, the white-line peaks of the spectra of both Pt_1/NCNS (Figure 7a) and Pt–SNs/NCNS (Figure 7c) are observed to shift toward higher energies with increasing applied potential, with Pt_1/NCNS shifting relatively more than Pt–SNs/NCNS. Importantly, from these chemical shifts it is concluded that the Pt oxidation state increased in both Pt_1/NCNS and Pt–SNs/NCNS. When reducing the applied potential from 1.1 V to 0.4 V, the oxidation state of Pt in Pt_1/NCNS was found to be still larger than that of Pt in Pt–SNs/NCNS. The EXAFS allowed to estimate a Pt–C/N/O coordination number on Pt_1/NCNS of 4.35 to 4.43 with a reverse shift of the potential from 1.1 V to 0.4 V (Figure 7b), while that on Pt–SNs/NCNS decreases from 2.28 to 1.72 (Figure 7d). The results of XANES and EXAFS remain in good agreement and revealed that the formation of stable PtO_x species on Pt_1/NCNS may further weaken the ability of O_2 adsorption and activation under ORR. Moreover, Cao et al. conducted in situ XAS measurements using a homemade cell in an O_2-saturated H_2SO_4 electrolyte to access atomic-level insights into the OER process occurring on a single-site Ru–N–C catalyst.[89] They observed that the first coordination peak showed a low-R shift of 0.07 Å at 1.5 V vs. RHE, along with the higher intensity in the FT-EXAFS curve of Ru–N–C catalyst under working conditions, suggesting the adsorption of oxygen-related species (Figure 7e). In situ XANES as shown in Figure 7f, compared with the RuO_2 octahedron, shows an apparent pre-edge characteristic feature at around 22115 eV, which is from the dipole-forbidden but quadrupole-allowed transition of Ru 1s to the unoccupied Ru 4d level under ex situ and open circuit conditions. Therefore, the unoccupied Ru 4d level observed in the ex situ XAS is the result of electron transfer from Ru 4d state to N 2p state via strong Ru–N hybridization in the Ru–N_4 sites, as shown in Figure 7g. However, under the working conditions of 1.5 V vs. RHE, this pre-edge peak intensifies compared to that recorded under open circuit conditions, indicating a distortion of the Ru coordination geometry and faster electron transfer from Ru 4d state to the nearby atoms under the working state, which may be induced by additional oxygen adsorption on Ru atoms as shown in Figure 7h. Thus, they considered that Ru atoms donate their electrons mainly to adjacent N atoms and the adsorbed O atom through orbital hybridization in O–Ru–N–C, resulting in a high OER activity.

4.2. Non-Noble Metal–N–C Materials

Noble metal-based ORR and OER electrocatalysts are highly active but suffer from high cost and scarcity of materials. Non-noble metal-based catalysts, especially transition metal–N–C materials, have attracted attention due to their environmental friendliness, low cost, high abundance, recyclability and durability. In situ XAS on these materials are reviewed in the following.

4.2.1. Fe–N–C Materials

Among the non-noble metal electrocatalysts reported to date, Fe-based catalysts are so far the most extensively studied.[56,67,90] To further improve the performance of Fe–N–C catalysts, in situ XAS techniques have been widely used to reveal the underlying evolution mechanism of their active centers as well as the ORR reaction pathways. For instance, Li et al. employed in situ XAS to explore the local structure of the active site of FePhenMOF–tArNH$_3$ catalyst under reaction conditions in an O_2/N_2-saturated 0.1 M perchloric acid ($HClO_4$) environment at room temperature.[91] Figure 8a shows that as the applied potential increases from 0.1 V to 1 V (vs. RHE), the primary peak of the catalyst roughly shifts from 7129 to 7133 eV. This chemical shift is related to the Fe^{2+}–tN_4/O_x–tFe^{3+}–tN_4 redox transition of the catalyst. They hypothesized that the active site is converted to the non-planar ferrous Fe–tN_4 moiety during the ORR at lower applied potentials, which aligns with FT-EXAFS and Δμ-XANES data. In addition, in situ Fe K-edge XAS collected in oxygen-free 0.1 M $HClO_4$ was used by Tylus and his co-workers as a control experiment to analyze the evolution of the active site and the mechanism of action of the M–N–C catalysts during the ORR.[37] As shown in Figure 8b, the in situ XANES spectra of the M–N–C catalyst shows that the Fe edge peak clearly shifts by about 2.5 eV to higher energies as the applied potential increases from 0.7 to 0.9 V, at which point the shift stops.

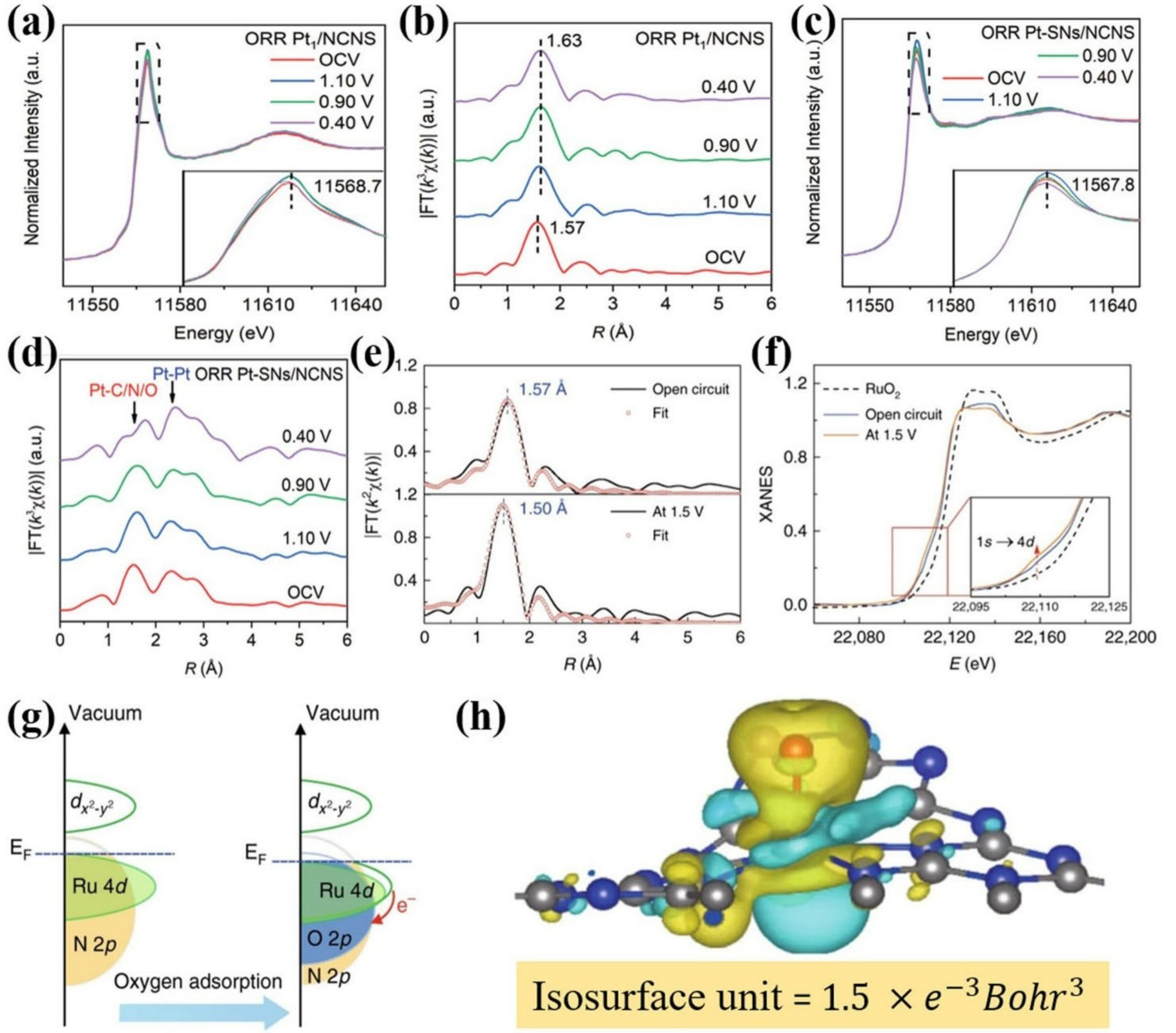

Figure 7. In situ XAS measurements of noble metal catalysts. XANES and EXAFS spectra at Pt L_3 edge for (a, b) Pt_1/NCNS and (c, d) Pt–SNs/NCNS recorded at different applied potentials from open circuit condition to 0.40 V during the ORR. Inset: zoomed in area corresponding to the white-line region indicated in a dotted box. (Reproduced with permission from [88], copyright 2021, WILEY-VCH Verlag GmbH & Co. KGaA, Weinheim). (e) EXAFS spectra and first-shell fitting curves for Ru–N–C at different applied voltages from the open circuit condition to 1.5 V during the OER, (f) XANES spectra for Ru–N–C recorded during the OER. Inset: magnified pre-edge XANES region, (g) Schematic illustration of the effect of oxygen adsorption on the electronic structure of Ru–N–C, (h) Electron density difference plot of the O–Ru_1–N_4. Yellow and light green contours represent electron accumulation and deletion, respectively. Spheres in gray, blue, red, white, and light green represent C, N, O, H, and Ru atoms, respectively. All potentials are indicated in the RHE scale. (Reproduced with permission from [89], copyright 2019, Springer Nature)

This means that the oxidation state of the Fe site increases, changing from Fe^{2+}–N_4 to Fe^{3+}–N_4. Furthermore, based on the in situ FT-EXAFS results (Figure 8c), the authors claim that O–Fe^{3+}–N_x are also generated in addition to the conversion from Fe^{2+}–N_4 to Fe^{3+}–N_4 as the potential increases from 0.7 to 0.9 V. The intensity of the peak positioned at 1.5 Å does not increase above 0.9 V because the oxide completely covers the Fe–N_4surface of the M–N–C catalyst. Combined with the ORR onset curves, they further concluded that hydroxyl species (OH^-) derived from water activation occupied the Fe–N_4 sites, thereby preventing molecular oxygen from adsorbing on the Fe–N_4sites.

Additionally, the catalytic principle of the Fe centers in a catalyst consisting of Fe SAs and Fe_2P nanoparticles (denoted as Fe SAs–tFe_2P NPs/NPCFs) during the ORR process was investigated by Pan et al. using potential-dependent in situ XAS in both acidic and alkaline media.[92] Fe K-edge XAS data for the Fe SAs–tFe_2P NPs/NPCFs-2.5 catalyst was acquired at different potentials in 0.5 M H_2SO_4 and 0.1 M KOH. In H_2SO_4, the in situ Fe K-edge XANES spectra (Figure 8d) exhibit that the prominent peak originat-

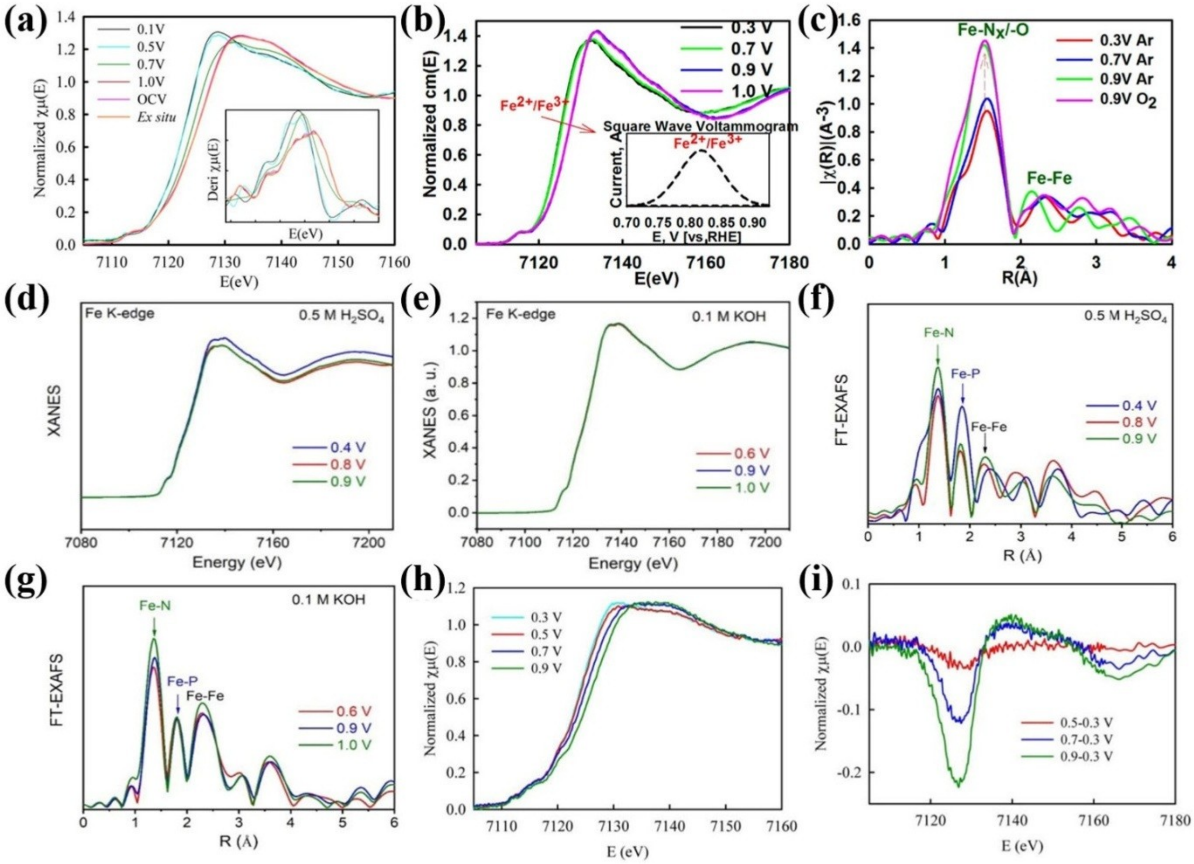

Figure 8. In situ XAS measurements at Fe K-edge. (a) Fe K-edge XANES of the FePhenMOF–tArNH$_3$ catalyst at different potentials in O$_2$/N$_2$-saturated 0.1 M HClO$_4$. (Reproduced with permission from [91], copyright 2016, The Royal Society of Chemistry). (b) Potential-dependent, normalized Fe K-edge XANES spectra with corresponding redox peak transition shown in inset as a background-subtracted square wave voltammetry profile collected in oxygen-free 0.1 M HClO$_4$, (c) in situ FT-EXAFS at the Fe K-edge (7112 eV) of PVAG–Fe catalyst. (Reproduced with permission from [37], copyright 2014, American Chemical Society). (d, e) In situ XANES spectra recorded at the Fe K-edge, and (f, g) corresponding k$_3$-weighted FT-EXAFS spectra of Fe SAs–tFe$_2$P NPs/NPCFs-2.5 at different applied voltages (vs. RHE) in 0.5 M H$_2$SO$_4$ and 0.1 M KOH, respectively. (Reproduced with permission from [92], copyright 2022, WILEY-VCH Verlag GmbH & Co. KGaA, Weinheim). (h) In situ Fe K-edge XANES, and (i) Δμ-XANES of the Fe–N–C-950 collected at 0.3–0.9 V in O$_2$/N$_2$-saturated electrolyte. (Reproduced with permission from [46], copyright 2018, American Chemical Society)

ing from the 1 s to 4p transition shifts to higher energies and decreases in intensity as the potential increases from 0.4 to 0.8 V (vs. RHE). The averaged oxidation state of iron increased with the applied potentials, reflecting the bonding of O* and OH* to the Fe site. From the in situ FT-EXAFS data in Figure 8f, it can be clearly seen that the peak at 1.85 Å assigned to Fe–N bonds does not change in intensity as strongly as the peak positioned at 1.91 Å assigned to Fe–P bonds, which further indicates that the adsorption and activation of O and OH are mainly controlled by the Fe–P site. In alkaline KOH, almost no difference can be seen at the Fe K-edge XANES of the catalyst as shown in Figure 8e except as the applied potential increases from 0.6 to 0.9 V vs. RHE. Compared with acidic media, in 0.1 M KOH, the Fe–O bond is perceptible but no pronounced change in the peak for the Fe–N bond at 1.85 Å is observed from the in situ FT-EXAFS results (Figure 8g), implying that Fe–P sites on the surface of the Fe SAs–tFe$_2$P NPs/NPCFs-2.5 catalyst do not actually participate in the O and OH absorption, while the FeN$_4$ moieties function as active sites during the ORR process in alkaline media. In H$_2$SO$_4$, the Fe–P sites of the Fe SAs–tFe$_2$P NPs/NPCFs-2.5 catalyst act as active sites for oxygen adsorption and activation, favouring the formation of P–Fe–O–H* intermediate species, thereby promoting the ORR process. In contrast, in KOH, the Fe–P sites fail during the ORR process, but the doping of P atoms changes the configuration of the Fe–N$_4$ moieties, thereby enhancing the ORR activity.

Another relevant example is found in the work of Xiao et al.[46] To examine the active site of a single-atom dispersed Fe–N–C electrocatalyst (Fe–N–C-950), in situ XAS techniques at Fe K-edge was employed, using O$_2$/N$_2$-saturated 0.1 M HClO$_4$solution at room temperature as electrolyte. The in situ Fe K-edge XANES results (Figure 8h) show that the peak at around 7117 eV, reflecting the electronic transition from 1 s to 3d, is not clearly identified, indicating that the catalyst is almost dominated by non-planar Fe–N$_4$ centers. As the applied potential increases from 0.3 to 0.9 V (vs. RHE), the main peak in the in situ XANES spectra exhibits a shift towards higher energies due to an increasing oxidation state of Fe. Further investigation shows that the corresponding amplitude of the main peak at 7126 eV gradually increased with the increase of the potential in the sine-like Δμ-XANES spectra (Figure 8i), which is highly consistent with the continuous conversion of Fe^{2+}–N_4 to O_x–Fe^{3+}–N_4 at high potentials. Combining the above results with the DFT and ex situ XAS data, the authors finally deduced that O_x–Fe^{3+}–N_4 of Fe–N–C-950 catalyst is reduced to HO-*Fe^{2+}–N_4 during the ORR process and acts as an active site to lower the reaction barrier.

4.2.2. Co–N–C Materials

Bifunctional oxygen electrodes are essential components in rechargeable metal-air batteries, as an OER-active material is required in the discharge state and an ORR-active material in the charge state. Co-based M–N–C catalysts are considered promising bifunctional oxygen catalysts by virtue of the multivalence feature of the Co element and the active metal-N_x centers with a carbonized ligand. Although the ORR activity of Co–N–C catalysts is slightly inferior to that of Fe-based SACs, their lower Fenton reaction activity promotes them to be excellent oxygen catalysts. The mechanism of oxygen binding sites on the Co center of pyrolyzed vitamin B_{12} (py-B12) during ORR was explained by Lien et al. in O_2-saturated 0.1 M $HClO_4$ environment under bias based on in situ XAS.[93] Figure 9a presents Co K-edge XANES spectra and the corresponding first-derivative spectra of py–B12. The highest point of the first derivative of each XANES spectrum is located at 7718.5 eV, which is interpreted as Co being mainly divalent in the ORR process. Further Δμ-XANES analysis at a bias of 0.6 V (vs. RHE) shows that the positive peak located at ≈7710 eV originates from the 1 s to 3d dipole transition of Co induced by the catalytic process related to the unfilled 3d orbital, and thus proves that the absorbed oxygen atom is coordinated in the edge-on position of the metal center. Moreover, the

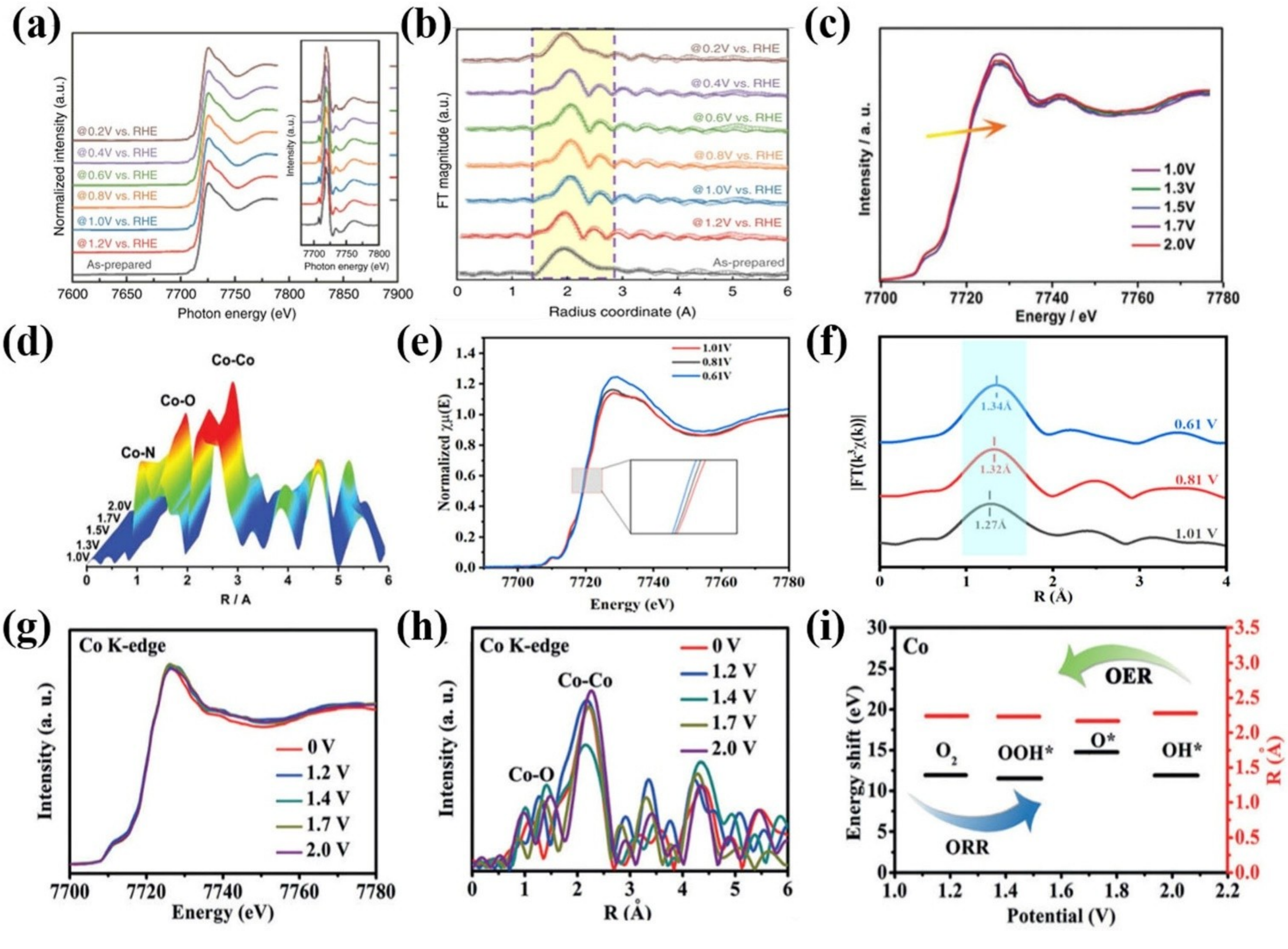

Figure 9. In situ XAS measurements at Co K-edge. (a) Co K-edge XANES and (b) phase-corrected FT-EXAFS spectra of py–B12 recorded at various electrode potentials. Inset shows the corresponding first-derivative spectra. (Reproduced with permission from [93], copyright 2020, Springer Nature). (c) XANES and (d) EXAFS at Co K-edge of Co/Co–N–C collected at different potentials. (Reproduced with permission from [38], copyright 2019, WILEY-VCH Verlag GmbH & Co. KGaA, Weinheim). (e) In situ XANES and (f) EXAFS spectra of Fe, Co SAs-PNCF recorded at various potentials during ORR. (Reproduced with permission from [94], copyright 2022, Elsevier). (g) In situ XANES and (h) FT-EXAFS spectra of the Co K-edge for CoFe/N-GCT collected at different potentials, (i) Changes in potential depicted for Co–Co bonds with respect to (g) energy shift and (h) bond length values. (Reproduced with permission from [67], copyright 2018, WILEY-VCH Verlag GmbH & Co. KGaA, Weinheim)

authors investigated the coordination of the metal centers during the catalytic process by in situ EXAFS. As shown in Figure 9b, the peak of the pristine catalyst at 1.95 Å indicates that the coordination number of the Co–N bond is 4. Applying a potential in the range from 1.0 to 0.4 V (vs. RHE) leads to a slight shift of the peak position until it stabilizes at 2.01 Å with Co–N coordination number of about 4. It is worth noting that, according to FT-EXAFS data, when the applied potential is in the range of 1.0 to 0.4 V (vs. RHE), the coordination number of the Co–O bond is 1.0, which indicates that a Co atom is bonded to only one oxygen species at the time. Thus, the authors explained the charge transfer effect existing between the reactants and the catalyst during the catalytic process by in situ XAS.

Additionally, the bifunctional ORR/OER catalytic mechanism of Co nanoislands rooted on Co–N–C nanosheets supported by carbon felts (Co/Co–N–C) in Zn-air batteries was systematically explained by Yu et al. using in situ XAS in an O_2-saturated 0.1 M KOH electrolyte environment.[38] As shown in Figure 9c, the main peak position of the in situ Co K-edge XANES spectra shifts to higher energies as the applied potential increases, indicating that the oxygen-containing species in the electrolyte participate in the coordination structure of the Co sites, thereby increasing the Co chemical valency. In situ FT-EXAFS observation at Co K-edge (Figure 9d) shows that the intensity of the peak representing Co–N bond at about 1.3 Å gradually increases with applied potential, while the intensities of the peaks representing Co–O bond and Co–Co bond at 1.5 Å and 2.2 Å, respectively, decreases, indicating the appearance of highly oxidized Co. The above observations reveal that the oxidation reactants are bonded to the Co sites on the Co/Co–N–C catalyst surface during the OER. In situ Co K-edge EXAFS fit shows that the bond lengths of Co–Co and Co–N bonds shorten as the applied potential increases, whereas the opposite is true for Co–O bonds. This result suggests that Co–Co bonds serve as active sites in the ORR reaction while Co–O bonds enhance the OER reaction during the dis-/charge process.

Due to the superior ORR activity of Fe-based catalysts, researchers attempted to embed Fe in Co–N–C catalyst to boost the ORR performance and achieve promising bifunctional catalysts supported by synergistic metal-metal interactions.[95] For instance, Jiang et al. studied the atomic-level insight of catalytic principles of atomic Fe/Co sites densely dispersed on porous nitrogen-doped carbon nanofibers (Fe, Co SAs-PNCF) during the ORR process in 0.1 M KOH electrolyte, and clarified its main active sites by means of in situ XAS as a function of applied potential.[94] The in situ XAS results at Co K-edge are shown in Figure 9e–f. As the applied potential is varied from 1.01 V to 0.61 V (vs. RHE), both the Co K-edge and Fe K-edge peaks in the corresponding in situ XANES spectra shift towards lower energies, which indicates that the oxidation states of Co and Fe gradually decrease. Based on the changes in the oxidation states, the authors inferred that atomic Fe acts as an active center for ORR, while Co is converted from CoOOH to $Co(OH)_2$. Furthermore, the in situ FT-EXAFS results indicate that the Co–N and Fe–N bonds are lengthened by about 5.51 % and 5.63 %, respectively, during the ORR process, suggesting $Fe–N_3$ in the Fe, Co SAs-PNCF catalyst assumes the role of the active site in the ORR process. Similarly, Liu et al. utilized in situ XAS-related techniques at the Co K-edge and the Fe K-edge to explore the catalytic mechanism of CoFe alloy nanoparticles supported on N-doped carbons catalyst (denoted as CoFe/N-GCT) during the ORR and the OER in the liquid Zn-air battery.[67] Figure 9g–i shows the in situ XAS results at Co K-edge. The in situ XANES spectra of both the Co and Fe K-edges exhibit a shift towards higher energies relative to their ex situ XANES spectra. Yet, neither the peak intensities nor the peak positions of the K-edges of Fe and Co present significant differences during the application of various potentials, indicating that as the applied potential changes during the ORR process, the dissolved oxygen in the electrolyte on the surface of CoFe/N-GCT is gradually converted into OOH*, O* and OH* species, and finally reduced to OH^-. In situ FT-EXAFS results at the Co and Fe K-edges show that as the applied potential increases from 0 V to 2.0 V (vs. RHE), the bond length of Fe–Fe bonds first elongates and then shortens, while the behavior of Co–Co bonds is diametrically reversed. This observation implies that the ORR and the OER occur on the surface of Fe and Co centers, respectively.

4.2.3. Ni–N–C Materials

Among earth-abundant transition metals, nickel (Ni) is one of the most favorable oxygen-evolving catalysts due to its desirable electrocatalytic activity and stability in alkaline electrolyte solutions.[9,96] Even though tremendous progress has been achieved in the past decade in the improvement of electrochemical performance of Ni–N–C-based oxygen catalysts, fundamental understanding of the structural dynamics and active sites of the electrocatalyst is still lacking.[12] In situ XAS has been employed to study electrocatalytic OER mechanisms by allowing the elucidation of the local atomic and electronic structure of the given element under reaction conditions,[2] which makes possible the exploration of scalable methods to synthesize high-performance Ni–N–C materials for oxygen electrocatalysis. For example, Su et al. adopted in situ XAS to reveal the dynamic evolution of the ORR active sites of Ni_1–NC SACs under electroreduction conditions using a homemade cell and O_2-saturated alkaline solution as electrolyte.[61] As shown in Figure 10a, the intensity of the characteristic peak at 8354 eV in the XANES spectra, corresponding to the electron transition from occupied Ni 2p to empty 3d states, gradually decreases as the reductive potential increases, indicating a potential-driven higher 3d occupancy for single Ni sites in the ORR. When the applied potential decreases from 0.95 to 0.70 V vs. RHE, the 8354 eV peak in the XANES of the Ni_1–NC catalysts distinctly splits into two different peaks, a and a′, with gradual attenuation in the peak intensity of both. Meanwhile, EXAFS spectra show a slightly positive shift of 0.05 Å for the peak centers as the applied potential

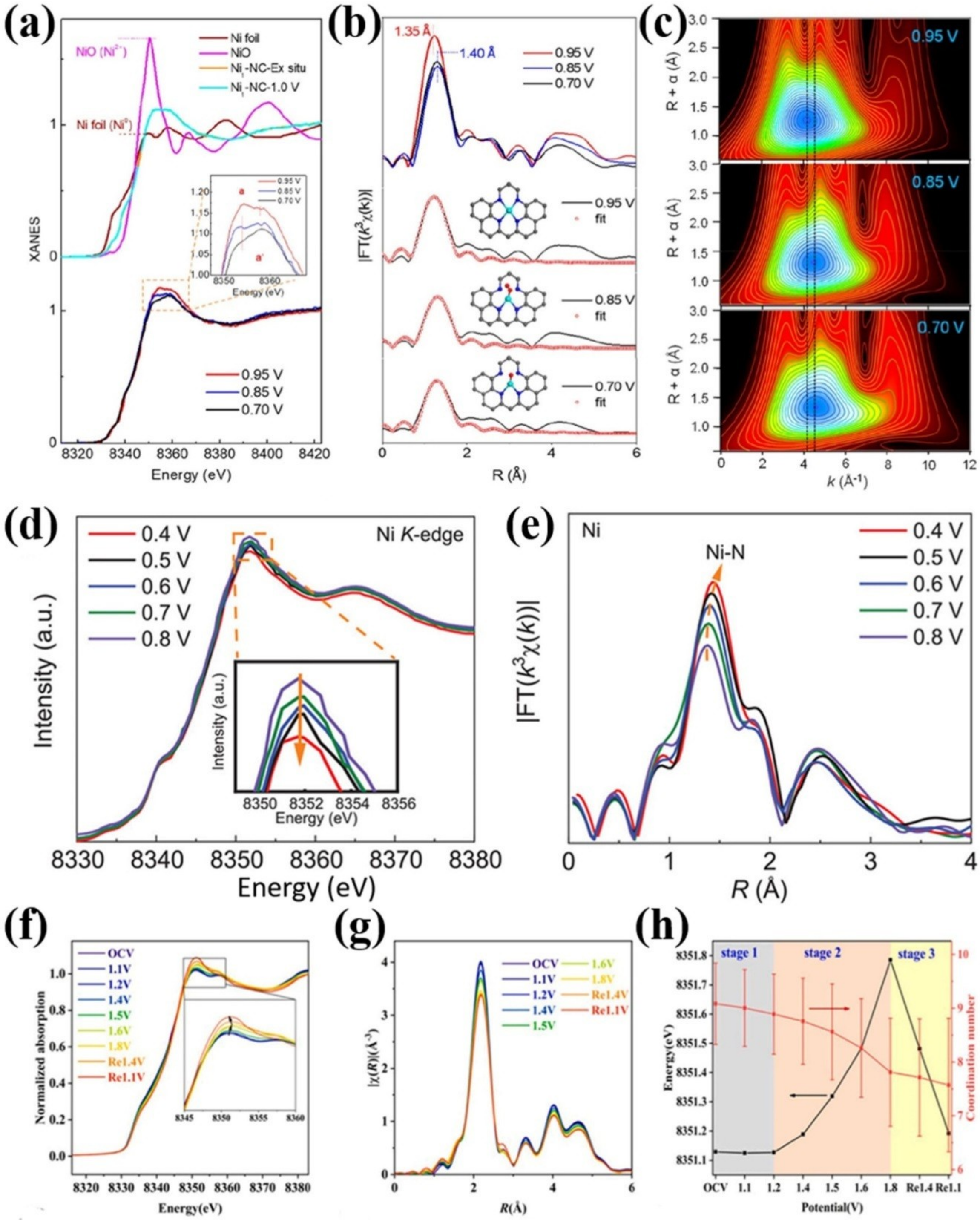

Figure 10. In situ XAS measurements at Ni K-edge. (a) Ni K-edge XANES spectra recorded at different potentials during the ORR, and the XANES data of the reference standards of Ni foil and NiO. The inset shows the magnified white-line region, (b) The first-shell fitting of EXAFS spectra under 0.95, 0.85 and 0.70 V vs. RHE. The insets show the corresponding geometric configurations, (c) Wavelet transforms for Ni_1–NC under 0.95, 0.85, and 0.70 V vs. RHE conditions. The vertical dashed lines are provided to guide the eye. (Reproduced with permission from [61], copyright 2020, American Chemical Society). (d) In situ Ni K-edge XANES spectra of NiZn MOF during ORR (inset shows the magnification of white-line region), (e) Corresponding in situ Ni K-edge EXAFS spectra for NiZn MOF at different applied potentials. (Reproduced with permission from [97], copyright 2022, WILEY-VCH Verlag GmbH & Co. KGaA, Weinheim). In situ XAS characterization analysis of Ni/NC-600 showing (f) Ni K-edge XANES spectra, (g) FT of k_2-weighted EXAFS, and (h) the energy shift of the main peak in XANES and fitting results of the CN in the first Ni–Ni shell. (Reproduced with permission from [98], copyright 2021, Elsevier)

decreased from 0.95 to 0.70 V vs. RHE, suggesting distinct variations in the local coordination environments of the Ni single sites during the ORR process. For Ni_1–NC at 0.85 V, the coordination number of the nearest Ni–N bonds is evidently reduced to 2 and the 2-fold Ni–N coordination combined with a Ni–O coordination of 1 is retained for the Ni single sites at 0.7 V (Figure 10b and 10c). These results confirmed that the potential-driven structural evolution of Ni single sites truly occurs under ORR conditions by releasing Ni centers from the N–C substrate to form a metastable and energetic near-free, isolated-zigzag $Ni_1^{(2-\delta)+}N_2$ active site with a much less coordinated and near-neutral atomic state structure, which dynamically favors the surface adsorption of oxygen molecules (O_2). Furthermore, Liu et al. employed in situ XAS to monitor the change of electronic structures and coordination environments of metal sites of as-prepared Ni–tM (M = Co, Cu, Zn) MOFs under ORR working conditions.[97] They found that the intensity of the characteristic overall white-line peak at 8351 eV of Ni K-edge XANES spectra gradually decreases with the applied voltages varying from 0.8 to 0.4 V vs. RHE, suggesting a potential-driven higher 3d occupancy for Ni sites in the ORR and thus indicating lower charge transfer from the Ni to nearby N atoms for a faster ORR process (Figure 10d). As the applied potential decreases from 0.8 to 0.6 V, the Ni–tN peak at around 1.40 Å in EXAFS spectra shifts from 1.38 to 1.45 Å, accompanied by an increased peak intensity, which may be induced by the emergence of *OOH intermediates over the Ni active sites during the ORR (Figure 10e). They considered that high-valence $Ni^{(2+\delta)+}$ sites act as the main active centers for the ORR via the 2-electron transfer pathway for H_2O_2 generation, which are essentially favorable for generating the key *OOH intermediate over $Ni^{(2+\delta)+}$ active sites. Similarly, in situ XAS was used by Zheng et al. to monitor the local structural evolution of the Ni sites in metallic Ni nanoparticles supported on N-doped carbon composites (Ni–N–C).[98] They found that, from 1.2 to 1.8 V vs. RHE, the main peak of XANES positioned at 8351.1 eV gradually shifts to 8351.8 eV (Figure 11f), indicating an increase in the Ni oxidation state, and subsequently returns close to its original position during the inverse process, and so does the oxidation state. Meanwhile, the main peaks in FT-EXAFS spectra are identical to the Ni foil reference but shift gradually with the increase of potential from 1.1 to 1.8 eV, as shown in Figure 10g and 11 h, demonstrating that the oxidation of the surface Ni atoms results in an apparent decrease of the average coordination numbers of metallic Ni. These results reveal the formation of $Ni(OH)_2$ on the surface at the initial stage and the reversible conversion to NiOOH in Ni–N–C materials.

4.2.4. Other Non-Noble Metal–N–C Materials

Atomically dispersed M–N–C materials based on other earth-abundant metals, including Cu–N–C and Mn–N–C, have been reported as promising oxygen electrocatalysts.[99] The evolution of Cu–N and Mn–N active sites during electrochemical processes has also been recently probed by in situ XAS.[12,16] Shang et al. employed in situ EXAFS to study the local atomic coordination evolution of the Mn sites in Mn SACs during the ORR and the OER.[53] The best-fitting analysis demonstrated that the optimized coordination arrangement in the working conditions (0.92 and 0.78 V vs. RHE for the ORR, 1.60 and 1.70 V vs. RHE for the OER) was the $Mn–N_2C_2$ moiety connected to oxygen intermediates (OOH*, O*, or OH*). The bond length is extended from 1.99 to 2.03 Å for Mn–N, and from 1.95 to 1.99 Å for Mn–C at 0.78 V during the ORR as shown in Figure 11a. However, during the OER, the bond lengths of Mn–N and Mn–C were shortened to 1.96 and 1.91 Å, respectively, at 1.70 V. Thus, confirming that the bond length-extended, low-valence $HOO–Mn–N_2C_2$, $O–Mn–N_2C_2$, and $HO–Mn–N_2C_2$ are likely the ORR active sites, while the oxygen-linked bond-length-shortened, high valence $Mn–N_2C_2$ OER species (Figure 11b). Additionally, in situ Cu K-edge XAS spectra were collected by Yang et al. in O_2-saturated 0.1 M KOH at different potentials (in the range from 0.00 to 1.10 V vs. RHE) to probe the evolution of the $Cu^{2+}–N_4$ structure in Cu–N–C materials.[78] Both the edge energy (E_0) and the white-line intensity (peak E) decrease as the cathodic potential increases, and concurrently a new peak (peak B), associated to the Cu^+ species, grows, indicating the gradual reduction of Cu^{2+} to Cu^+ during the ORR process (Figure 11c). The XAS collected at 0.82, 0.50, and 0.10 V are best fitted with $Cu–N_4$, $Cu–N_3$, and $Cu–N_2–OH$ (Figure 11d–11 f), respectively, suggesting that the catalyst likely consists of more than one $Cu–N_x$ structure at the different potentials, with the dominant structures shown in the insets. With an increase in the cathodic potential to 0.50 and 0.10 V, a higher amount of Cu^{2+} species are reduced to Cu^+, which is accompanied by the structural evolution from $Cu–N_4$ to $Cu–N_3$ and finally to $Cu–N_2$. Thus, based on these results, the dynamic evolution of $Cu–N_4$ to $Cu–N_3$ and further to $HO–Cu–N_2$ under the working conditions of the ORR was identified. The increase in the Cu^+/Cu^{2+} ratio with the increase of cathodic potential indicates that the low-coordinated $Cu^+–N_3$ is the real active site. Another relevant example was presented by Shang et al., who carried out in situ Cu K-edge XAS measurements of S–Cu-ISA/SNC in 0.1 M KOH to monitor the structural evolution of the isolated copper sites during the ORR.[100] When the applied potential was reversed from 0.75 to 1.05 V, the edge position shifted back to higher energies along with an increase in the intensity of the white-line peak, displaying potential-dependent oxidation (Figure 11g). Meanwhile, k_3-weighted FT-EXAFS spectra for S–Cu-ISA/SNC collected at 0.90 V and 0.75 V vs. RHE exhibited one main peak (Cu–N) along with a shoulder peak (Cu–S) as shown in Figure 11h. However, under the working condition, the Cu–N peaks shifted their position from 1.55 to 1.49 Å, implying that the local structure of the active site was changed, which was monitored through the shrinking of Cu–N bond length. These results support the electronic and atomic structure evolution of the $Cu–S_1N_3$ moiety in S–Cu-ISA/SNC, and revealed that the shrinking of the low-valence

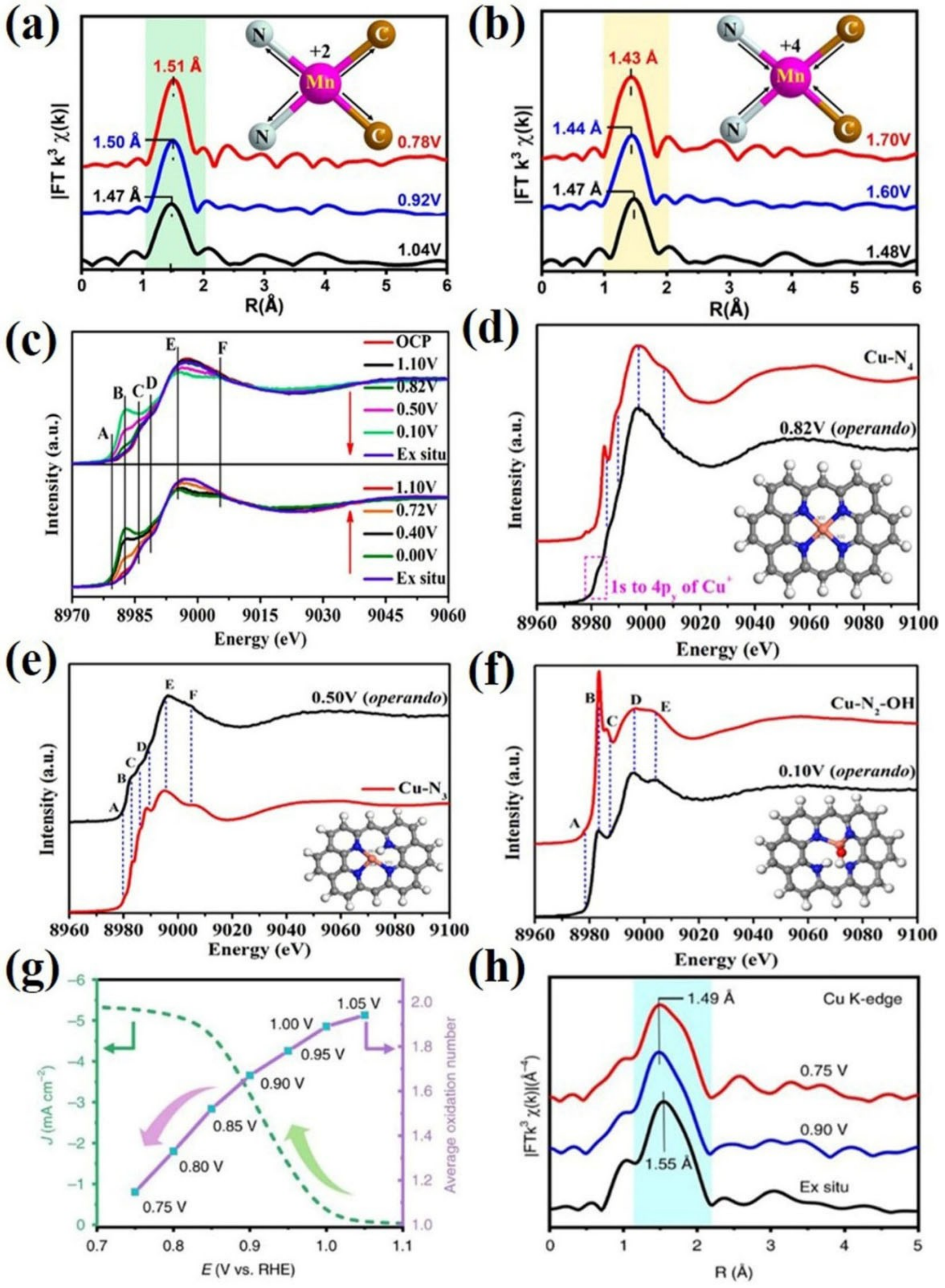

Figure 11. In situ XAS characterization of Mn SACs. The EXAFS spectra of Mn SACs during (a) ORR and (b) OER. (Reproduced with permission from [53], copyright 2020, American Chemical Society). (c) In situ XANES spectra recorded in the Cu K-edge in the cathodic (top) and anodic directions (bottom), (d) Comparison between the Cu K-edge XANES spectrum recorded at 0.82 V vs. RHE (black line) and the theoretical Cu–N$_4$ XANES spectrum (red line). The peak highlighted by a dashed rectangle is the 1 s to 4py transition of Cu$^+$, (e) Comparison between Cu K-edge XANES spectra recorded at 0.50 V (black line) and theoretical Cu–N$_3$ XANES spectra (red line), (f) comparison between Cu K-edge XANES spectra recorded at 0.10 V (black line) and theoretical Cu–N$_2$–OH XANES spectra (red line). Insets in (e) and (f) are their corresponding models. (Reproduced with permission from [78], copyright 2021, American Chemical Society). (g) Current density as a function of potential for S–Cu–ISA/SNC (left) and the average oxidation number of Cu species in S–Cu–ISA/SNC as a function of applied potential (right), (h) k_3-weighted FT-EXAFS collected ex situ, at 0.90 V and at 0.75 V vs. RHE. The shaded region highlights the variations in the peak position of the first coordination shell. (Reproduced with permission from [100], copyright 2020, Springer Nature)

Cu–N-bond species HOO–Cu–S_1N_3, O–Cu–S_1N_3 and HO–Cu–S_1N_3 might contribute to its high ORR activity.

4.3. Comparison of active sites of ORR and OER M–N–C electrocatalysts identified by in situ XAS

An overview of the active sites of ORR and OER M–N–C electrocatalysts identified by in situ XAS are summarized in Table 2. Most studies listed here have targeted the metal K-edges. In general, by fitting in situ EXAFS at the K-edge, the coordination configurations with N and C as well as the change of bond length during working conditions can be analyzed. Nonetheless, it is worth noting that the metal L-edge can also reflect the local chemical environment of these metals. From these results, it is clear that the active sites of Fe–N–C and Co–N–C materials are mostly in the form of Fe–N_x and Co–N_x moieties while Ni–N–C materials prefer to form $Ni^{(2\text{-}\delta)+}N_x$as active sites for ORR.[61] Yet, it is important to consider that a general understanding of the nature of active sites in M–N–C-type materials is presently limited, not only due to the technical difficulties inherent to in situ XAS experiments, but also to the differences in the experimental conditions of the electrochemical experiments themselves. As shown in Table 2, such differences include electrode preparation methods, electrolyte composition, mass transport conditions and range of applied potentials, in addition to the cell configuration as discussed in Section 3. Furthermore, the effect of doping an M–N–C matrix with heteroatoms additional to N should be carefully considered when comparing M–N–C materials, as the additional heteroatom probably induces a new active site, for example, the active site of Cu–S_1N_3 where one N atom is replaced by one S atom compared to Cu–N_x active sites.[100] Nevertheless, there is no doubt that in situ XAS methods help accelerate the improvement of M–N–C oxygen electrocatalysts by enabling the identification of active sites.

5. Summary and Outlook

The emergence of M–N–C materials, including single-atom catalysts, over the past decade has reinvigorated research efforts targeting the discovery of low-cost electrocatalysts for the conversion of oxygen (ORR and OER).[2,82] On account of their unique quantum size effects, maximized metal atom utilization, tunable metal-support interactions, high interfacial contact with the electrolyte, and high electrical conductivity, M–N–C electrocatalysts have not only been investigated to advance fundamental scientific understanding of active site chemistry, but have also emerged as a class of highly promising electrocatalysts for sustainable electrochemical energy conversion technologies, including electrolyzers, fuel cells and (rechargeable) metal-air batteries.[101] Nevertheless, some ambiguity still remains in regard to the formation mechanisms of metal-N_X moieties within the carbon matrix, or the origin of the OER/ORR activity on metal-metal/metal-N_X sites. Although advanced techniques, such as FT-IR spectroscopy, Raman spectro-

Table 2: Summary of the active sites of typical ORR and OER M–N–C catalysts identified by in situ XAS and their details of measurement conditions.

Working electrode	Counter electrode	Reference electrode	Electrolyte	Reaction	Measurement mode	Targeted edge	Active sites	Ref.
Pt_1–N–C on carbon paper taped with Kapton film	Carbon paper	Ag/AgCl	O_2-saturated 0.5 M H_2SO_4	ORR, 0.4–1.1 V vs. RHE	Fluorescence mode	Pt L_3-edge	PtO_x species	[88]
Ru–N–C on carbon cloth taped with Kapton film	Carbon cloth	Ag/AgCl	O_2-saturated 0.5 M H_2SO_4	OER, 1.2–1.6 V vs. RHE	Fluorescence mode	Ru K-edge	O–Ru_1–N_4	[89]
MOF-derived Fe–N–C coated on carbon cloth taped with a piece of heated glass	Carbon cloth	Ag/AgCl	O_2-saturated 0.1 M $HClO_4$	ORR, 0.1–1.0 V vs. RHE	Fluorescence mode	Fe K-edge	Fe–tN_4 moiety	[91]
Fe SAs–tFe_2P NPs/NPCFs coated with graphite powder	Graphite powder	Ag/AgCl	O_2-saturated 0.5 M H_2SO_4 and 1 M KOH	ORR, 0.4–1.0 V vs. RHE	Fluorescence mode	Fe K-edge	Fe–N_4 moiety	[92]
Microporous framework derived Fe–N–C	–	Ag/AgCl	O_2-saturated 0.1 M $HClO_4$	ORR, 0.3–0.9 V vs. RHE	Fluorescence mode	Fe K-edge	Fe^{2+}–N_4	[46]
Co/Co–N–C on carbon felt	Carbon felts	Ag/AgCl	O_2-saturated 0.1 M KOH	OER and ORR, 1.0 –2.0 V vs. RHE	Fluorescence mode	Co K-edge	Co–Co and Co–N bonds for ORR; Co–O bond for OER	[38]
Ni_1–N–C on carbon cloth taped with Kapton film	Carbon cloths	Ag/AgCl	O_2-saturated 0.1 M NaOH	ORR, 0.7–1.0 V vs. RHE	Fluorescence mode	Ni K-edge	$Ni_1^{(2\text{-}\delta)+}N_2$	[61]
Mn–N–C on carbon cloth in contact with copper tape	Platinum rod	$Hg/HgCl_2$	O_2-saturated 0.1 M KOH	OER and ORR, 0.7–1.7 V vs. RHE	Fluorescence mode	Mn K-edge	Low-valence HOO–Mn–N_2C_2, O–Mn–N_2C_2, and HO–Mn–N_2C_2 for ORR;High valence Mn–N_2C_2 species for OER	[53]
S–Cu–ISA/SNC on carbon paper	Graphite rod	Ag/AgCl	O_2-saturated 0.1 M KOH	ORR, 0.75–1.05 V vs. RHE	Fluorescence mode	Cu K-edge	Cu–S_1N_3	[100]

scopy, UV/Vis spectroscopy and DFT methods, have helped to elucidate the catalytic reactions, the role of metal and metal-N_x configurations in the reaction mechanisms has been only partially revealed.[15,102] In situ XAS techniques are advantageous for monitoring changes in the chemical state as well as the structural evolution of catalysts under reaction conditions due to its sensitivity to the valence and local structure of selected elements.[103] A better understanding of the nature of active sites will enable the establishment of structure-property-performance relationships, which are needed for further design of high-performance catalytic materials.[12]

In this review, we comprehensively introduced in situ XAS as a powerful tool for the investigation of M–N–C-based oxygen electrocatalysts. A discussion on active sites and structural evolution of M–N–C-based catalysts under reaction conditions was then presented. Finally, we reviewed recent advances in the investigation of M–N–C-based oxygen electrocatalysts by in situ XAS. Although great progress has been made over the past few years in developing in situ XAS for the study of electrocatalysts for energy applications related to ORR and OER, challengesremain for the identification of active sites and structural evolution of M–N–C materials. These are summarized below:

1. In situ XAS provides insight into the average structural changes of metal-metal/metal-Nx active sites rather than individual active centers.. The catalytic reactions of M–N–C materials occur primarily on the surface, where reactants can efficiently absorb on the active sites. Thus, improving XAS detection schemes with surface-sensitivity is crucial for better comprehension of the performance of M–N–C electrocatalysts.[104] Such surface and near-surface sensitivity can be achieved by decreasing the particle size, employing $\Delta\mu$ analysis, designing core–shell configurations of M–N–C materials, and carefully ensuring that the full thickness of the M–N–C samples is electrochemically accessible and active.[32]
2. Despite the application of in situ XAS to observe the origin and evolution of catalytic sites at an atomic level, further development has been hindered by complex operational requirements of the experimental equipment, leading to limited spectroscopic evidence on electronic and geometric structures of active sites.[104] Additionally, in situ XAS investigations have not yet been able to fully elucidate the mechanisms of targeted catalytic reactions because of large dissimilarities in final outcomes, including valence state, metal-N_x coordination, and electronic structure of metals, achieved by various research laboratories under similar experimental conditions. Conflicting experimental results stem from the complexity of the experimental operation for in situ XAS, including technical challenges to achieve sufficiently thin electrolyte layers, the impact of gas input (in ORR) or gas evolution (in OER) on both the surface of the catalyst and on the optical membrane for in situ detection, as well as precise control of purity of experimental environment and quality of X-ray beamline. Consequently, experimental setups for in situ XAS need more optimization to identify active sites reliably in M–N–C-based oxygen catalysts.[105]
3. The inability to identify coordination to atoms with similar masses, particularly the electrocatalytic C, N, and O atoms, remains a problem when employing in situ EXAFS methods to characterize electrocatalytic materials.[106] In situ N K-edge XAS under electrochemical conditions remains challenging due to strong background signal from the silicon nitride membranes and possible contamination in the beamline. Instead, in situ XAS focuses on the metal K-edge or metal L-edge.[107] Metal L-edge spectra describe the transitions of 2p electrons to unfilled d-orbitals. Oxidation state changes of metal sites are better revealed by exploring the L-edge of transition metal by in situ soft XAS.[107] Future advances significantly depend on innovative X-ray analysis and corresponding in situ techniques for exploring the oxygen states of M–N–C materials during electrocatalysis. However, there are still numerous technical problems, such as the requirement of ultrahigh vacuum conditions and the need for a flow cell with a continuous input of electrolyte in a sealed chamber. In situ soft XAS at the O K-edge might become increasingly popular to identify oxygen redox reactions of electrocatalysts at different electrochemical states in real time by probing the degree of hybridization of the metal-oxygen bonds.[108] Although soft X-rays impose making the study of catalytic reactions challenging, in situ soft XAS shows great promise as a tool to probe the oxygen-involved chemical state of M–N–C catalysts and the coordinated atoms.[107] Therefore, the development of in situ XAS at the C, N, or O K-edge and metal L-edge requires more attention to allow the characterization of oxygen electrocatalysis.[32]
4. Presently, in situ XAS research on oxygen electrocatalysis is mainly confined to examining the electrode structure at a specific applied potential.. Considering that the electrode structure is highly sensitive to the applied potential, it is necessary to devise rational strategies to select suitable potential ranges for measuring and monitoring the dynamic electrode structure during potential cycling.[106] Moreover, the current in situ XAS studies on M–N–C oxygen electrocatalysis have solely been conducted in half-cell configurations to concentrate on electrolyte-electrode interfaces, whereas real electrochemical devices, such as fuel cells and metal-air batteries, follow a membrane-electrode assembly structure that encompasses multiple parameters to determine overall electrocatalytic OER/ORR performance. Therefore, more effort on designing of practical device-based in situ electrochemical cells should be made soon, with detailed measurement protocols established.
5. Time-resolved XAS can be easily implemented by recording intensity changes at fixed excitation energy to separate changes of the oxidation states in terms of non-catalytic processes from those occurring during catalysis of M–N–C materials.[14] This approach can be either applied to record XAS during cyclic voltammetry or to record transients during potentiostatic measurements[14]

to identify the redox states involved in the OER and ORR of M–N–C samples.

6. Spatially resolved studies, as well as experiments that combine spatial mapping with time-resolved investigations of the catalyst dynamics, are also expected to gain importance in the future. Particularly, synchrotron X-ray absorption edge imaging with high energy resolution was applied to study aging of fuel cell catalyst materials. The imaging and high X-ray energy resolution setup combination enabled the acquisition of spatially resolved XAS (XANES and EXAFS) spectra, allowing for visual local chemical information through targeted element imaging.[109] This method partially overcomes one of the XAS method's most significant limitations, which is its sample-averaging nature. We believe that the potential of such experiments is currently severely underexploited. Despite the fact that proof-of-concept spatially resolved XAS studies of electrocatalysis have been carried out in the recent decade, the practical application of this approach to oxygen electrocatalysis, especially on M–N–C-based oxygen catalysts is still missing.[110]

From this review it should be evident that regardless of the continuous efforts to decipher the working mechanism of M–N–C catalysts, many questions still need to be addressed. Further, thanks to the research directed toward the development of more sensitive and highly effective in situ XAS-based characterization techniques, we believe that the most exciting contributions to unravel the working mechanisms of M–N–C-based electrocatalysts in OER/ORR are yet to come. Despite the associated challenges, this field remains very exciting and in its early stages. We therefore hope that this review can persuade a new generation of catalysis scientists and X-ray spectroscopists to work on this topic.

Acknowledgements

This work was funded by the National Natural Science Foundation of China (Grant Nos. 51902238, 52127816), the Fundamental Research Funds for the Central Universities (WUT: 2020IVA069), and the China Postdoctoral Science Foundation-funded project (2020M670343). This work was also supported by the Volkswagen Foundation (Freigeist Fellowship No. 89592). The authors acknowledge support from Shanghai Synchrotron Radiation Facility (SSRF), China and Berlin Synchrotron Radiation Source-BESSY II, Germany and thank Prof. Simone Raoux from Helmholtz-Zentrum Berlin für Materialien und Energie GmbH for her linguistic modifications during the preparation of this manuscript. Open Access funding enabled and organized by Projekt DEAL.

Conflict of Interest

The authors declare no conflict of interest.

Keywords: Active Sites · In Situ XAS · M–N–C Catalysts · Oxygen Electrocatalysis · Structural Evolution

---

[1] Z.-L. Wang, D. Xu, J.-J. Xu, X.-B. Zhang, *Chem. Soc. Rev.* **2014**, *43*, 7746–7786.
[2] B. Wu, H. Meng, D. M. Morales, F. Zeng, J. Zhu, B. Wang, M. Risch, Z. J. Xu, T. Petit, *Adv. Funct. Mater.* **2022**, *32*, 2204137–2204173.
[3] J.-L. Shui, N. K. Karan, M. Balasubramanian, S.-Y. Li, D.-J. Liu, *J. Am. Chem. Soc.* **2012**, *134*, 16654–16661.
[4] L. Peng, Z. Wei, *Engineering* **2020**, *6*, 653–679.
[5] Q. Shi, C. Zhu, D. Du, Y. Lin, *Chem. Soc. Rev.* **2019**, *48*, 3181–3192.
[6] L. Li, P. Wang, Q. Shao, X. Huang, *Adv. Mater.* **2021**, *33*, 2004243–2004267.
[7] Q. Liu, M. Ranocchiari, J. A. van Bokhoven, *Chem. Soc. Rev.* **2022**, *51*, 188–236.
[8] S. Zhang, S. Chen, *J. Power Sources* **2013**, *240*, 60–65.
[9] M. Zhang, H. Li, J. Chen, F.-X. Ma, L. Zhen, Z. Wen, C.-Y. Xu, *Small* **2022**, *18*, 2202476--2202186.
[10] Y. J. Sa, D.-J. Seo, J. Woo, J. T. Lim, J. Y. Cheon, S. Y. Yang, J. M. Lee, D. Kang, T. J. Shin, H. S. Shin, H. Y. Jeong, C. S. Kim, M. G. Kim, T.-Y. Kim, S. H. Joo, *J. Am. Chem. Soc.* **2016**, *138*, 15046–15056.
[11] A. D. Handoko, F. Wei, Jenndy, B. S. Yeo, Z. W. Seh, *Nat. Catal.* **2018**, *1*, 922–934.
[12] J. Timoshenko, B. Roldan Cuenya, *Chem. Rev.* **2021**, *121*, 882–961.
[13] S. J. L. Billinge, I. Levin, *Science* **2007**, *316*, 561–565.
[14] M. Risch, D. M. Morales, J. Villalobos, D. Antipin, *Angew. Chem. Int. Ed.* **2022**, *61*, e202211949; *Angew. Chem.* **2022**, *134*, e202211949.
[15] S. Chen, L. Ma, Z. Huang, G. Liang, C. Zhi, *Cell Rep. Phys. Sci.* **2022**, *3*, 100729–100762.
[16] E. M. Erickson, M. S. Thorum, R. Vasić, N. S. Marinković, A. I. Frenkel, A. A. Gewirth, R. G. Nuzzo, *J. Am. Chem. Soc.* **2012**, *134*, 197–200.
[17] D. M. Koshy, A. T. Landers, D. A. Cullen, A. V. Ievlev, H. M. Meyer, C. Hahn, Z. Bao, T. F. Jaramillo, *Adv. Energy Mater.* **2020**, *10*, 2001836–2001845.
[18] D. Saurel, A. Pendashteh, M. Jáuregui, M. Reynaud, M. Fehse, M. Galceran, M. Casas-Cabanas, *Chem. Methods* **2021**, *1*, 249–260.
[19] S. Zhao, Y. Yang, Z. Tang, *Angew. Chem. Int. Ed.* **2022**, *61*, e202110186; *Angew. Chem.* **2022**, *134*, e202110186.
[20] L. Zhang, H. Jang, H. Liu, M. G. Kim, D. Yang, S. Liu, X. Liu, J. Cho, *Angew. Chem. Int. Ed.* **2021**, *60*, 18821–18829; *Angew. Chem.* **2021**, *133*, 18969–18977.
[21] K. F. Kalz, R. Kraehnert, M. Dvoyashkin, R. Dittmeyer, R. Gläser, U. Krewer, K. Reuter, J.-D. Grunwaldt, *ChemCatChem* **2017**, *9*, 17–29.
[22] P. A. Lee, P. H. Citrin, P. Eisenberger, B. M. Kincaid, *Rev. Mod. Phys.* **1981**, *53*, 769–806.
[23] E. L. Shirley, J. C. Woicik, *Phys. Chem. Chem. Phys.* **2022**, *24*, 20742–20759.
[24] M. Newville, *Rev. Mineral. Geochem.* **2014**, *78*, 33–74.
[25] G. La Penna, V. Minicozzi, S. Morante, G. C. Rossi, F. Stellato, *J. Chem. Phys.* **2015**, *143*, 124508–124515.
[26] T. Yamamoto, *X-Ray Spectrom.* **2008**, *37*, 572–584.
[27] M. L. Baker, M. W. Mara, J. J. Yan, K. O. Hodgson, B. Hedman, E. I. Solomon, *Coord. Chem. Rev.* **2017**, *345*, 182–208.
[28] Y. Xu, F. Li, A. Xu, J. P. Edwards, S.-F. Hung, C. M. Gabardo, C. P. O'Brien, S. Liu, X. Wang, Y. Li, J. Wicks, R. K. Miao, Y. Liu, J. Li, J. E. Huang, J. Abed, Y. Wang, E. H. Sargent, D. Sinton, *Nat. Commun.* **2021**, *12*, 2932–2939.

[29] H. Zhao, R. Yu, S. Ma, K. Xu, Y. Chen, K. Jiang, Y. Fang, C. Zhu, X. Liu, Y. Tang, L. Wu, Y. Wu, Q. Jiang, P. He, Z. Liu, L. Tan, *Nat. Catal.* **2022**, *5*, 818–831.

[30] J. Ohyama, M. Moriya, R. Takahama, K. Kamoi, S. Kawashima, R. Kojima, T. Hayakawa, Y. Nabae, *JACS Au* **2021**, *1*, 1798–1804.

[31] K. Ebner, A. H. Clark, V. A. Saveleva, G. Smolentsev, J. Chen, L. Ni, J. Li, A. Zitolo, F. Jaouen, U. I. Kramm, T. J. Schmidt, J. Herranz, *Adv. Energy Mater.* **2022**, *12*, 2103699-2103713.

[32] H. Huang, A. E. Russell, *Curr. Opin. Electrochem.* **2021**, *27*, 100681–100691.

[33] N. Watanabe, J. Morais, M. C. M. Alves, *J. Electron Spectrosc. Relat. Phenom.* **2007**, *156–158*, 164–167.

[34] J. W. Smith, R. J. Saykally, *Chem. Rev.* **2017**, *117*, 13909–13934.

[35] O. Proux, E. Lahera, W. Del Net, I. Kieffer, M. Rovezzi, D. Testemale, M. Irar, S. Thomas, A. Aguilar-Tapia, E. F. Bazarkina, A. Prat, M. Tella, M. Auffan, J. Rose, J.-L. Hazemann, *J. Environ. Qual.* **2017**, *46*, 1146–1157.

[36] D. Asakura, E. Hosono, Y. Nanba, H. Zhou, J. Okabayashi, C. Ban, P.-A. Glans, J. Guo, T. Mizokawa, G. Chen, A. J. Achkar, D. G. Hawthron, T. Z. Regier, H. Wadati, *AIP Adv.* **2016**, *6*, 035105–035113.

[37] U. Tylus, Q. Jia, K. Strickland, N. Ramaswamy, A. Serov, P. Atanassov, S. Mukerjee, *J. Phys. Chem. C* **2014**, *118*, 8999–9008.

[38] P. Yu, L. Wang, F. Sun, Y. Xie, X. Liu, J. Ma, X. Wang, C. Tian, J. Li, H. Fu, *Adv. Mater.* **2019**, *31*, 1901666–1901675.

[39] A. J. Achkar, T. Z. Regier, H. Wadati, Y.-J. Kim, H. Zhang, D. G. Hawthorn, *Phys. Rev. B* **2011**, *83*, 081106–081110.

[40] L. C. Colocho Hurtarte, L. F. Souza-Filho, W. Oliveira Santos, L. Vergütz, J. Prietzel, D. Hesterberg, *Soil Systems* **2019**, *3*, 61–74.

[41] C. J. Pelliccione, E. V. Timofeeva, J. P. Katsoudas, C. U. Segre, *J. Phys. Chem. C* **2013**, *117*, 18904–18912.

[42] M. Mannini, F. Pineider, P. Sainctavit, C. Danieli, E. Otero, C. Sciancalepore, A. M. Talarico, M.-A. Arrio, A. Cornia, D. Gatteschi, R. Sessoli, *Nat. Mater.* **2009**, *8*, 194–197.

[43] B. H. Frazer, B. Gilbert, B. R. Sonderegger, G. De Stasio, *Surf. Sci.* **2003**, *537*, 161–167.

[44] S. L. M. Schroeder, G. D. Moggridge, E. Chabala, R. M. Ormerod, T. Rayment, R. M. Lambert, *Faraday Discuss.* **1996**, *105*, 317–336.

[45] D. Vlachos, A. J. Craven, D. W. McComb, *J. Synchrotron Radiat.* **2005**, *12*, 224–233.

[46] M. Xiao, J. Zhu, L. Ma, Z. Jin, J. Ge, X. Deng, Y. Hou, Q. He, J. Li, Q. Jia, S. Mukerjee, R. Yang, Z. Jiang, D. Su, C. Liu, W. Xing, *ACS Catal.* **2018**, *8*, 2824–2832.

[47] M. J. Dzara, K. Artyushkova, M. T. Sougrati, C. Ngo, M. A. Fitzgerald, A. Serov, B. Zulevi, P. Atanassov, F. Jaouen, S. Pylypenko, *J. Phys. Chem. C* **2020**, *124*, 16529–16543.

[48] F. W. Lytle, P. S. P. Wei, R. B. Greegor, G. H. Via, J. H. Sinfelt, *J. Chem. Phys.* **1979**, *70*, 4849–4855.

[49] I. J. Drake, T. C. N. Liu, M. Gilles, T. Tyliszczak, A. L. D. Kilcoyne, D. K. Shuh, R. A. Mathies, A. T. Bell, *Rev. Sci. Instrum.* **2004**, *75*, 3242–3247.

[50] L. Cao, X. Liu, X. Shen, D. Wu, T. Yao, *Acc. Chem. Res.* **2022**, *55*, 2594–2603.

[51] Y. Yang, Y. Wang, Y. Xiong, X. Huang, L. Shen, R. Huang, H. Wang, J. P. Pastore, S.-H. Yu, L. Xiao, J. D. Brock, L. Zhuang, H. D. Abruña, *J. Am. Chem. Soc.* **2019**, *141*, 1463–1466.

[52] M. Görlin, J. Halldin Stenlid, S. Koroidov, H.-Y. Wang, M. Börner, M. Shipilin, A. Kalinko, V. Murzin, O. V. Safonova, M. Nachtegaal, A. Uheida, J. Dutta, M. Bauer, A. Nilsson, O. Diaz-Morales, *Nat. Commun.* **2020**, *11*, 6181–6192.

[53] H. Shang, W. Sun, R. Sui, J. Pei, L. Zheng, J. Dong, Z. Jiang, D. Zhou, Z. Zhuang, W. Chen, J. Zhang, D. Wang, Y. Li, *Nano Lett.* **2020**, *20*, 5443–5450.

[54] X. Li, C.-S. Cao, S.-F. Hung, Y.-R. Lu, W. Cai, A. I. Rykov, S. Miao, S. Xi, H. Yang, Z. Hu, J. Wang, J. Zhao, E. E. Alp, W. Xu, T.-S. Chan, H. Chen, Q. Xiong, H. Xiao, Y. Huang, J. Li, T. Zhang, B. Liu, *Chem* **2020**, *6*, 3440–3454.

[55] X. Duan, S. Ren, N. Pan, M. Zhang, H. Zheng, *J. Mater. Chem. A* **2020**, *8*, 9355–9363.

[56] A. I. Douka, H. Yang, L. Huang, S. Zaman, T. Yue, W. Guo, B. You, B. Y. Xia, *EcoMat* **2021**, *3*, 12067–12085.

[57] X. Zheng, X. Cao, Z. Sun, K. Zeng, J. Yan, P. Strasser, X. Chen, S. Sun, R. Yang, *Appl. Catal. B* **2020**, *272*, 118967–118994.

[58] M. Tong, F. Sun, Y. Xie, Y. Wang, Y. Yang, C. Tian, L. Wang, H. Fu, *Angew. Chem. Int. Ed.* **2021**, *60*, 14005–14012; *Angew. Chem.* **2021**, *133*, 14124–14131.

[59] N. Zhang, T. Zhou, J. Ge, Y. Lin, Z. Du, C. Zhong, W. Wang, Q. Jiao, R. Yuan, Y. Tian, W. Chu, C. Wu, Y. Xie, *Matter* **2020**, *3*, 509–521.

[60] L. Song, Y. Cai, Y. Liu, X. Zhao, K. A. Kuttiyiel, N. Marinkovic, A. I. Frenkel, A. Kongkanand, Y. Choi, R. R. Adzic, K. Sasaki, *ACS Appl. Bio Mater. ACS Appl. Energ. Mater.* **2022**, *5*, 5245–5255.

[61] H. Su, W. Zhou, H. Zhang, W. Zhou, X. Zhao, Y. Li, M. Liu, W. Cheng, Q. Liu, *J. Am. Chem. Soc.* **2020**, *142*, 12306–12313.

[62] Y. He, Q. Shi, W. Shan, X. Li, A. J. Kropf, E. C. Wegener, J. Wright, S. Karakalos, D. Su, D. A. Cullen, G. Wang, D. J. Myers, G. Wu, *Angew. Chem. Int. Ed.* **2021**, *60*, 9516–9526; *Angew. Chem.* **2021**, *133*, 9602–9612.

[63] Z. Lu, B. Wang, Y. Hu, W. Liu, Y. Zhao, R. Yang, Z. Li, J. Luo, B. Chi, Z. Jiang, M. Li, S. Mu, S. Liao, J. Zhang, X. Sun, *Angew. Chem. Int. Ed.* **2019**, *58*, 2622–2626; *Angew. Chem.* **2019**, *131*, 2648–2652.

[64] S. Seok, M. Choi, Y. Lee, D. Jang, Y. Shin, Y.-H. Kim, C. Jo, S. Park, *ACS Appl. Nano Mater.* **2021**, *4*, 9418–9429.

[65] N. Yu, H. Chen, J. Kuang, K. Bao, W. Yan, J. Ye, Z. Yang, Q. Huang, Y. Wu, S. Sun, *Nano Res.* **2022**, *15*, 7209–7219.

[66] K. R. Yoon, C.-K. Hwang, S. Kim, J.-W. Jung, J. E. Chae, J. Kim, K. A. Lee, A. Lim, S.-H. Cho, J. P. Singh, J. M. Kim, K. Shin, B. M. Moon, H. S. Park, H.-J. Kim, K. H. Chae, H. C. Ham, I.-D. Kim, J. Y. Kim, *ACS Nano* **2021**, *15*, 11218–11230.

[67] X. Liu, L. Wang, P. Yu, C. Tian, F. Sun, J. Ma, W. Li, H. Fu, *Angew. Chem. Int. Ed.* **2018**, *57*, 16166–16170; *Angew. Chem.* **2018**, *130*, 16398–16402.

[68] N. Zhang, T. Zhou, M. Chen, H. Feng, R. Yuan, C. Zhong, W. Yan, Y. Tian, X. Wu, W. Chu, C. Wu, Y. Xie, *Energy Environ. Sci.* **2020**, *13*, 111–118.

[69] S. Ma, Z. Han, K. Leng, X. Liu, Y. Wang, Y. Qu, J. Bai, *Small* **2020**, *16*, 2001384–2001391.

[70] X. Li, X. Yang, L. Liu, H. Zhao, Y. Li, H. Zhu, Y. Chen, S. Guo, Y. Liu, Q. Tan, G. Wu, *ACS Catal.* **2021**, *11*, 7450–7459.

[71] T. Cui, Y.-P. Wang, T. Ye, J. Wu, Z. Chen, J. Li, Y. Lei, D. Wang, Y. Li, *Angew. Chem. Int. Ed.* **2022**, *61*, e202115219; *Angew. Chem.* **2022**, *134*, e202115219.

[72] L. Xu, Y. Tian, D. Deng, H. Li, D. Zhang, J. Qian, S. Wang, J. Zhang, H. Li, S. Sun, *ACS Appl. Mater. Interfaces* **2020**, *12*, 31340–31350.

[73] J. Chen, H. Li, C. Fan, Q. Meng, Y. Tang, X. Qiu, G. Fu, T. Ma, *Adv. Mater.* **2020**, *32*, 2003134–2003145.

[74] F. Luo, J. Zhu, S. Ma, M. Li, R. Xu, Q. Zhang, Z. Yang, K. Qu, W. Cai, Z. Chen, *Energy Storage Mater.* **2021**, *35*, 723–730.

[75] H. Li, Y. Wen, M. Jiang, Y. Yao, H. Zhou, Z. Huang, J. Li, S. Jiao, Y. Kuang, S. Luo, *Adv. Funct. Mater.* **2021**, *31*, 2011289–2011302.

[76] W. Luo, Y. Wang, L. Luo, S. Gong, M. Wei, Y. Li, X. Gan, Y. Zhao, Z. Zhu, Z. Li, *ACS Catal.* **2022**, *12*, 1167–1179.

[77] L. Hu, C. Dai, L. Chen, Y. Zhu, Y. Hao, Q. Zhang, L. Gu, X. Feng, S. Yuan, L. Wang, B. Wang, *Angew. Chem. Int. Ed.* **2021**, *60*, 27324–27329; *Angew. Chem.* **2021**, *133*, 27530–27535.

[78] J. Yang, W. Liu, M. Xu, X. Liu, H. Qi, L. Zhang, X. Yang, S. Niu, D. Zhou, Y. Liu, Y. Su, J.-F. Li, Z.-Q. Tian, W. Zhou, A. Wang, T. Zhang, *J. Am. Chem. Soc.* **2021**, *143*, 14530–14539.

[79] D. Xue, P. Yuan, S. Jiang, Y. Wei, Y. Zhou, C.-L. Dong, W. Yan, S. Mu, J.-N. Zhang, *Nano Energy* **2023**, *105*, 108020–108030.

[80] L. Li, Y.-J. Chen, H.-R. Xing, N. Li, J.-W. Xia, X.-Y. Qian, H. Xu, W.-Z. Li, F.-X. Yin, G.-Y. He, H.-Q. Chen, *Nano Res.* **2022**, *15*, 8056–8064.

[81] S. Zaman, Y.-Q. Su, C.-L. Dong, R. Qi, L. Huang, Y. Qin, Y.-C. Huang, F.-M. Li, B. You, W. Guo, Q. Li, S. Ding, B. Yu Xia, *Angew. Chem. Int. Ed.* **2022**, *61*, e202115835; *Angew. Chem.* **2022**, *134*, e202115835.

[82] J. Zhang, Y. Zhao, C. Chen, Y.-C. Huang, C.-L. Dong, C.-J. Chen, R.-S. Liu, C. Wang, K. Yan, Y. Li, G. Wang, *J. Am. Chem. Soc.* **2019**, *141*, 20118–20126.

[83] L. Yang, X. Zhang, L. Yu, J. Hou, Z. Zhou, R. Lv, *Adv. Mater.* **2022**, *34*, 2105410–2105420.

[84] Q. Huang, B. Wang, S. Ye, H. Liu, H. Chi, X. Liu, H. Fan, M. Li, C. Ding, Z. Li, C. Li, *ACS Catal.* **2022**, *12*, 491–496.

[85] E. Fabbri, D. F. Abbott, M. Nachtegaal, T. J. Schmidt, *Curr. Opin. Electrochem.* **2017**, *5*, 20–26.

[86] Y. Chen, S. Ji, C. Chen, Q. Peng, D. Wang, Y. Li, *Joule* **2018**, *2*, 1242–1264.

[87] W. Ma, H. Wan, L. Zhang, J. Y. Zheng, Z. Zhou, *J. Energy Chem.* **2021**, *63*, 170–194.

[88] J. Li, M. N. Banis, Z. Ren, K. R. Adair, K. Doyle-Davis, D. M. Meira, Y. Z. Finfrock, L. Zhang, F. Kong, T. Sham, R. Li, J. Luo, X. Sun, *Small* **2021**, *17*, 2007245–2007253.

[89] L. Cao, Q. Luo, J. Chen, L. Wang, Y. Lin, H. Wang, X. Liu, X. Shen, W. Zhang, W. Liu, Z. Qi, Z. Jiang, J. Yang, T. Yao, *Nat. Commun.* **2019**, *10*, 4849–4858.

[90] B. Y. Xia, Y. Yan, N. Li, H. B. Wu, X. W. (David). Lou, X. Wang, *Nat. Energy* **2016**, *1*, 15006–15014.

[91] J. Li, S. Ghoshal, W. Liang, M.-T. Sougrati, F. Jaouen, B. Halevi, S. McKinney, G. McCool, C. Ma, X. Yuan, Z.-F. Ma, S. Mukerjee, Q. Jia, *Energy Environ. Sci.* **2016**, *9*, 2418–2432.

[92] Y. Pan, X. Ma, M. Wang, X. Yang, S. Liu, H. Chen, Z. Zhuang, Y. Zhang, W. Cheong, C. Zhang, X. Cao, R. Shen, Q. Xu, W. Zhu, Y. Liu, X. Wang, X. Zhang, W. Yan, J. Li, H. M. Chen, C. Chen, Y. Li, *Adv. Mater.* **2022**, *34*, 2203621–2203636.

[93] H.-T. Lien, S.-T. Chang, P.-T. Chen, D. P. Wong, Y.-C. Chang, Y.-R. Lu, C.-L. Dong, C.-H. Wang, K.-H. Chen, L.-C. Chen, *Nat. Commun.* **2020**, *11*, 4233–4241.

[94] M. Jiang, F. Wang, F. Yang, H. He, J. Yang, W. Zhang, J. Luo, J. Zhang, C. Fu, *Nano Energy* **2022**, *93*, 106793–106803.

[95] H. Jin, S. Mao, G. Zhan, F. Xu, X. Bao, Y. Wang, *J. Mater. Chem. A* **2017**, *5*, 1078–1084.

[96] K. S. Anuratha, M. Rinawati, T.-H. Wu, M.-H. Yeh, J.-Y. Lin, *Nanomaterials* **2022**, *12*, 2970–3008.

[97] M. Liu, H. Su, W. Cheng, F. Yu, Y. Li, W. Zhou, H. Zhang, X. Sun, X. Zhang, S. Wei, Q. Liu, *Small* **2022**, *18*, 2202248–2201255.

[98] Y. Zheng, G. Zhang, P. Zhang, S. Chu, D. Wu, C. Sun, B. Qian, S. Chen, S. Tao, L. Song, *Chem. Eng. J.* **2022**, *429*, 132122–132130.

[99] A. Kumar, V. K. Vashistha, D. K. Das, S. Ibraheem, G. Yasin, R. Iqbal, T. A. Nguyen, R. K. Gupta, Md. Rasidul Islam, *Fuel* **2021**, *304*, 121420–121435.

[100] H. Shang, X. Zhou, J. Dong, A. Li, X. Zhao, Q. Liu, Y. Lin, J. Pei, Z. Li, Z. Jiang, D. Zhou, L. Zheng, Y. Wang, J. Zhou, Z. Yang, R. Cao, R. Sarangi, T. Sun, X. Yang, X. Zheng, W. Yan, Z. Zhuang, J. Li, W. Chen, D. Wang, J. Zhang, Y. Li, *Nat. Commun.* **2020**, *11*, 3049–3060.

[101] M. Hu, S. Li, S. Zheng, X. Liang, J. Zheng, F. Pan, *J. Phys. Chem. C* **2020**, *124*, 13168–13176.

[102] L. Liu, W. Li, X. He, J. Yang, N. Liu, *Small* **2022**, *18*, 2104205–2104227.

[103] A. Beheshti Askari, M. al Samarai, B. Morana, L. Tillmann, N. Pfänder, A. Wandzilak, B. Watts, R. Belkhou, M. Muhler, S. DeBeer, *ACS Catal.* **2020**, *10*, 6223–6230.

[104] M. Wang, L. Árnadóttir, Z. J. Xu, Z. Feng, *Nano-Micro Lett.* **2019**, *11*, 47–65.

[105] M. V. Varsha, G. Nageswaran, *Front. Chem.* **2020**, *8*, 23–35.

[106] S.-F. Hung, *Pure Appl. Chem.* **2020**, *92*, 733–749.

[107] Y. Yang, I. Roh, S. Louisia, C. Chen, J. Jin, S. Yu, M. B. Salmeron, C. Wang, P. Yang, *J. Am. Chem. Soc.* **2022**, *144*, 8927–8931.

[108] F. Frati, M. O. J. Y. Hunault, F. M. F. de Groot, *Chem. Rev.* **2020**, *120*, 4056–4110.

[109] T. Arlt, I. Manke, K. Wippermann, H. Riesemeier, J. Mergel, J. Banhart, *J. Power Sources* **2013**, *221*, 210–216.

[110] Y.-C. Feng, X. Wang, Y.-Q. Wang, H.-J. Yan, D. Wang, *J. Electrochem.* **2022**, *28*, 2108531–2108544.

Manuscript received: December 27, 2022
Accepted manuscript online: February 17, 2023
Version of record online: April 17, 2023